# A TIR-1/SARM1 phase transition underlies p38 immune pathway activation in the *C. elegans* intestine

**Nicholas D. Peterson[1,#], Janneke D. Icso [2,#], J. Elizabeth Salisbury[1], Tomás Rodríguez[3], Paul R. Thompson[2,*], Read Pukkila-Worley[1,*]**

[1]Program in Innate Immunity, Division of Infectious Diseases and Immunology, [2]Department of Biochemistry and Molecular Pharmacology, [3]RNA Therapeutics Institute, University of Massachusetts Medical School, Worcester, MA, 01655, United States of America

#These authors contributed equally to this work

*Correspondence may be addressed to Read Pukkila-Worley (Read.Pukkila-Worley@umassmed.edu, @RPWlab) or Paul Thompson (Paul.Thompson@umassmed.edu, @pthompsn1018)

Classification: Major: Biological Sciences; Minor: Immunology and Inflammation

Keywords: p38 pathway; cholesterol; TIR-1/SARM1; phase transition

**ABSTRACT**

Intracellular signaling regulators can be concentrated into membrane-free, higher-ordered protein assemblies to initiate protective responses during stress — a process known as phase transition. Here, we show that a phase transition of the *Caenorhabditis elegans* Toll/interleukin-1 receptor domain protein (TIR-1), an $NAD^+$ glycohydrolase homologous to mammalian sterile alpha and TIR motif-containing 1 (SARM1), underlies p38 PMK-1 immune pathway activation in *C. elegans* intestinal epithelial cells. Through visualization of fluorescently labeled TIR-1/SARM1 protein, we demonstrate for the first time that physiologic stresses, both pathogen and non-pathogen, induce multimerization of TIR-1/SARM1 into visible puncta within intestinal epithelial cells. *In vitro* enzyme kinetic analyses revealed that, like mammalian SARM1, the $NAD^+$ glycohydrolase activity of *C. elegans* TIR-1 is dramatically potentiated by protein oligomerization and a phase transition. Accordingly, *C. elegans* with genetic mutations that specifically block either multimerization or the $NAD^+$ glycohydrolase activity of TIR-1/SARM1 fail to induce p38 PMK phosphorylation, are unable to increase immune effector expression, and are dramatically susceptible to bacterial infection. Finally, we demonstrate that the TIR-1/SARM1 phase transition is modified by dietary cholesterol, revealing a new adaptive response that allows a metazoan host to anticipate pathogen threats during micronutrient deprivation, a time of relative susceptibility to infection. When cholesterol is limited, TIR-1/SARM1 oligomerizes into puncta in intestinal epithelial cells and engages its $NAD^+$ glycohydrolase activity, which increases p38 PMK-1 phosphorylation, and primes immune effector induction in a manner that promotes pathogen clearance from the intestine during a subsequent infection. Thus, a phase transition of TIR-1/SARM1 as a prerequisite for its $NAD^+$ glycohydrolase activity is strongly conserved across millions of years of evolution and is essential for diverse physiological processes in multiple cell types.

47 **INTRODUCTION**

48 The p38 mitogen-activated protein kinase (MAPK) pathway is a key regulator of stress
49 responses and innate immune defenses in metazoans. The *C. elegans* p38 homolog PMK-1 is
50 part of a classic MAPK signaling cascade that is activated by the MAPKKK NSY-1 and MAPKK
51 SEK-1, which are the nematode homologs of mammalian ASK and MKK3/6, respectively [1]. *C.*
52 *elegans* Toll/interleukin-1 receptor domain protein (TIR-1), an $NAD^+$ glycohydrolase homologous
53 to mammalian sterile alpha and TIR motif-containing 1 (SARM1), acts upstream of NSY-1 to
54 control p38 PMK-1 activation [2, 3]. As in mammals, the *C. elegans* p38 PMK-1 pathway regulates
55 the expression of secreted innate immune effectors and is required for survival during pathogen
56 infection [1, 4-6]. However, the mechanisms that activate the NSY-1/SEK-1/p38 PMK-1 signaling
57 cassette in *C. elegans* intestinal epithelial cells are poorly defined.

58 Intracellular signaling regulators can be compartmentalized in membrane-less, higher-
59 ordered protein assemblies with liquid droplet-like properties [7-13]. Cytoplasmic de-mixing or
60 phase transition of proteins in this manner concentrates signaling regulators to facilitate rapid and
61 specific activation of protective defenses during stress [7, 8, 14]. Here, we show that a phase
62 transition and $NAD^+$ glycohydrolase activity of TIR-1/SARM1 is required for p38 PMK-1 immune
63 pathway activation in *C. elegans* intestinal epithelial cells. By promoting aggregation of TIR-
64 1/SARM1 with macromolecular crowding agents *in vitro*, we demonstrate that a phase transition
65 is required for the catalytic activity of TIR-1/SARM1. Accordingly, TIR-1/SARM1 containing
66 mutations that either specifically prevent the phase transition or impair $NAD^+$ hydrolysis show
67 decreased enzymatic activity *in vitro*. *C. elegans* carrying these same mutations, edited into the
68 genome using CRISPR/Cas9, fail to induce p38 PMK phosphorylation, are unable to upregulate
69 immune effector expression, and have enhanced susceptibility to bacterial infection. Importantly,
70 we labeled the TIR-1/SARM1 protein with a fluorescent tag at its genomic locus and demonstrated
71 for the first time that TIR-1/SARM1 oligomerizes into visible puncta within the intestine in response
72 to physiologic stimuli, including both a pathogen and non-pathogen stress.

73 In a contemporaneous study, Loring et al. demonstrated that human SARM1 aggregates
74 and undergoes a phase transition to potentiate its intrinsic $NAD^+$ glycohydrolase activity [15].
75 These authors studied SARM1 in the context of neuronal degeneration as it was previously
76 demonstrated that loss of mammalian SARM1 protects against axonal degeneration following
77 neuronal injury [16-18]. Treatment with non-physiologic concentrations of citrate, a molecule that
78 induces protein aggregation, led to oligomerization of *C. elegans* TIR-1 in neurons, which was
79 correlated with enhanced axonal degeneration [15]. We demonstrate here that *C. elegans* TIR-
80 1/SARM1 oligomerizes to form puncta in response to physiological stresses, providing an
81 important characterization of the mechanism inferred by Loring, et al., and establish that the TIR-
82 1/SARM1 phase transition occurs in non-neuronal tissues in the regulation of intestinal immunity.
83 Thus, a phase transition of TIR-1/SARM1 as a prerequisite for its $NAD^+$ glycohydrolase activity is
84 strongly conserved, occurs in multiple cell types, and is essential for diverse physiological
85 processes, including intestinal immune regulation and axonal degeneration.

86 Finally, we report that a non-pathogen stress can induce TIR-1/SARM1 oligomerization
87 and p38 PMK-1 pathway activation as part of a mechanism to preempt pathogen attack during a
88 time of relative vulnerability to infection. *C. elegans* lack the ability to synthesize cholesterol *de*
89 *novo* and must acquire dietary sterols from its environment to support multiple aspects of cellular
90 physiology, including development, fecundity, lifespan, and resistance against pathogen infection
91 [19-25]. Some, but not all, *C. elegans* larvae that encounter sterol-scarce environments enter an
92 alternative developmental program, called dauer diapause, to promote animal survival [26-30].
93 Here, we show that *C. elegans* that do not enter dauer diapause in an environment devoid of
94 dietary sterols adapt by promoting oligomerization of TIR-1/SARM1 to activate the p38 PMK-1
95 innate immune pathway. Otarigho et al. previously demonstrated that dietary cholesterol is
96 required for *C. elegans* to survive infection with the bacterial pathogen *Pseudomonas aeruginosa*
97 and argued that cholesterol is necessary for the induction of some innate immune response
98 pathways in nematodes [24]. Surprisingly, we found in multiple genome-wide transcriptome

99 profiling experiments that *C. elegans* in a low cholesterol environment robustly activate, rather
100 than repress, the transcription of a suite of genes, the majority of which are innate immune
101 effectors that are downstream of the p38 PMK-1 pathway. We confirmed in genetic epistasis and
102 western blot experiments that low cholesterol activates the TIR-1/NSY-1/SEK-1/p38 PMK-1
103 pathway in the absence of infection. Importantly, we show that priming p38 pathway activation in
104 this manner augments immune effector expression during a subsequent bacterial infection and
105 promotes pathogen clearance from the intestine. Thus, activation of the p38 PMK-1 pathway
106 during conditions of low cholesterol availability is an adaptive response that allows nematodes to
107 anticipate pathogen threats under conditions of essential metabolite scarcity.

108 **RESULTS**

109 **Cholesterol scarcity activates intestinal innate immune defenses.**

110 *C. elegans* are sterol auxotrophs and require dietary sterols for development, lifespan,
111 fecundity, and resistance to pathogen infection [19-25]. As such, 5 µg/mL of cholesterol is a
112 standard additive in *C. elegans* laboratory growth medium [31]. We found that *C. elegans* grown
113 in the absence of cholesterol supplementation activated GFP-based transcriptional reporters for
114 two putative immune effector genes, T24B8.5p::*gfp* and *irg-5*p::*gfp* (Figs. 1A and B). T24B8.5 and
115 *irg-5* are expressed in the intestine, induced during infection with multiple pathogens, including *P.*
116 *aeruginosa,* and controlled by the p38 PMK-1 innate immune pathway [4, 32, 33]. qRT-PCR
117 studies confirmed that *C. elegans* in a low cholesterol environment upregulate T24B8.5 and *irg-*
118 *5,* as well as other innate immune effector genes (*irg-4* and K08D8.4) (Fig. 1C). These data
119 suggest that host defense pathways are activated in the absence of pathogen infection when
120 environmental sterols are scarce.

121 The nuclear hormone receptor, NHR-8, a homolog of mammalian liver X receptor (LXR)
122 and pregnane X receptor (PXR), is required for the transport, distribution, and metabolism of
123 cholesterol in *C. elegans* [34, 35]. Thus, *nhr-8* loss-of-function mutant strains can be used as
124 genetic tools to study conditions of low sterol content. Two previously-characterized *nhr-8* null
125 alleles are *nhr-8(hd117)*, which lacks the first exon [34] and *nhr-8(ok186)*, which is missing most
126 of the ligand-binding domain [35]. Notably, the transcription profile of *nhr-8(hd117)* and *nhr-*
127 *8(ok186)* animals mimics that of wild-type *C. elegans* infected with the bacterial pathogen *P.*
128 *aeruginosa* (Figs. 1D, S1A, Table S1A, and Table S1B). The correlation between the
129 transcriptional signatures of either the *nhr-8(hd117)* or the *nhr-8(ok186)* mutant with the genes
130 that are changed in wild-type animals during pathogen infection was significant across all genes
131 (r = 0.311 and r = 0.370, respectively). Of note, the correlation between these datasets is tighter
132 when comparing only the differentially expressed genes (r = 0.763 and r = 0.849, respectively)
133 and only genes that are also involved in innate immunity (r = 0.677 and r = 0.703, respectively)

134 (Figs. 1D and S1A). Among the immune effectors that are upregulated in both the *nhr-8(hd117)*
135 and *nhr-8(ok186)* mutants, and in wild type animals infected with *P. aeruginosa,* are T24B8.5, *irg-*
136 *4*, *irg-5*, and K08D8.4; the same genes whose transcription are also induced by cholesterol
137 deprivation (Figs. 1C, 1D and S1A).

138 To validate these findings, we analyzed publicly available RNA-seq data that compared
139 gene expression changes in wild-type *C. elegans* grown in media lacking supplemented
140 cholesterol versus animals grown under standard culture conditions with 5 μg/mL of cholesterol
141 [24]. Consistent with our transcriptome profiling experiments of *nhr-8* loss-of-function mutants, we
142 found that innate immune effectors were strongly enriched among genes that were
143 transcriptionally activated during cholesterol deprivation (Fig. 1E). Specifically, the expression of
144 innate immune effectors was significantly correlated in wild-type animals infected with *P.*
145 *aeruginosa* and in wild-type nematodes starved for cholesterol (r = 0.361) (Fig. 1E). Immune
146 effectors that were induced during cholesterol starvation in qRT-PCR studies (*irg-4*, *irg-5* and
147 K08D8.4, but not T24B8.5) were again found among these differentially regulated genes,
148 confirming the integrity of our RNA-seq analysis (Fig. 1C). In summary, cholesterol-starved, wild-
149 type *C. elegans* and two different *nhr-8* loss-of-function mutants induce the transcription of innate
150 immune defenses.

151 Two different supplementation experiments using the T24B8.5p::*gfp* immune reporter
152 demonstrated that immune effector activation in *nhr-8(hd117)* mutants is due to sterol deficiency
153 in these animals. First, supplementation of exogenous cholesterol at an increased concentration
154 (80 μg/mL) fully suppressed T24B8.5p::*gfp* activation in the *nhr-8(hd117)* mutant (Fig. 1F).
155 Second, supplementation with the non-ionic detergents Tergitol or Triton X-100, which solubilize
156 hydrophobic, amphipathic compounds, including sterols, suppressed T24B8.5p::*gfp* activation in
157 *nhr-8(hd117)* animals in a manner that was dependent on the presence of added cholesterol in
158 the growth media (Figs. 1G, 1H and S1B). Nematode growth media solidified with agarose, rather
159 than agar, contains markedly fewer contaminating sterols [20, 28, 34]. Importantly, on agarose,

160 the addition of Tergitol to the growth media also suppressed T24B8.5p::*gfp* activation in the *nhr-*
161 *8(hd117)* mutant, but only in the presence of 5 µg/mL of cholesterol (Fig. 1H). Notably, this effect
162 was dose-dependent (Fig. S1B). These data establish that solubilization of cholesterol by Tergitol
163 in standard nematode growth media suppresses immune activation in the *nhr-8(hd117)* mutant
164 background. We used qRT-PCR to confirm these findings – Tergitol suppressed activation of
165 T24B8.5, as well as the immune effectors *irg-4*, *irg-5* and K08D8.4 in the *nhr-8(hd117)* mutant
166 (Figs. 1I-L). Of note, activation of immune defenses in *nhr-8(hd117)* animals is specific to
167 cholesterol deprivation in this genetic background, as supplementation with individual
168 unsaturated, mono- and polyunsaturated fatty acids, which are also mis-regulated in the *nhr-*
169 *8(hd117)* mutant background [34], failed to suppress activation of T24B8.5p::*gfp* (Fig. S1C).
170 Together, these data confirm that cholesterol deprivation activates immune effector transcription
171 independent of bacterial infection.

172 It has been previously shown that *C. elegans* raised on media without supplemented
173 cholesterol are hypersusceptible to killing by *P. aeruginosa*, as are *nhr-8(hd117)* mutants on
174 media with standard cholesterol supplementation (5 µg/mL) [24]. Importantly, we found that high
175 doses of cholesterol (80 µg/mL) rescued the enhanced susceptibility of *nhr-8(hd117)* mutants to
176 *P. aeruginosa* infection (Fig. 1M). We confirmed this finding in an orthologous approach. Two
177 detergents (Tergitol or Triton X-100), which solubilize cholesterol in nematode growth media, also
178 restored wild-type pathogen resistance to the *nhr-8(hd117)* mutant (Fig. 1N), consistent with their
179 ability to modulate the expression of innate immune effectors (Fig. 1G-L). Thus, cholesterol is
180 required for pathogen resistance in *C. elegans*.

181 Importantly, we found that the robust transcriptional induction of immune effectors
182 observed in the *nhr-8(hd117)* mutant promotes clearance of *P. aeruginosa* from the intestine (Fig.
183 1O). Thus, even though *nhr-8(hd117)* mutant animals are more susceptible to pathogen killing,
184 they are mounting effective anti-pathogen defenses toward an ingested pathogen (Fig. 1O).
185 These data suggest that *C. elegans* activates host immune defenses when environmental sterols

186 are limited to preempt pathogen attack during a period of relative susceptibility to bacterial
187 infection.
188
189 **Cholesterol scarcity activates the p38 PMK-1 innate immune pathway.**
190 Additional analyses of the transcriptome profiling data revealed that targets of the p38
191 PMK-1 innate immune pathway were strongly enriched among the genes induced in wild-type
192 animals during cholesterol deprivation (Fig. 2A). Consistent with this observation, the levels of
193 active, phosphorylated PMK-1 were higher in wild-type animals grown on media without
194 supplemented cholesterol than in animals grown under standard culture conditions (Figs. 2B and
195 2C). These data demonstrate that cholesterol deprivation activates p38 PMK-1.
196 The p38 PMK-1 pathway is also activated in *nhr-8* loss-of-function mutants. A gene set
197 enrichment analysis of the *nhr-8(hd117)* and *nhr-8(ok186)* transcriptome profiling experiments
198 revealed strong enrichment of p38 PMK-1 pathway targets among the genes upregulated in each
199 *nhr-8* mutant (Figs. 2D and S2A). Consistent with these data, the *nhr-8(hd117)* and *nhr-8(ok186)*
200 mutants had an increased ratio of phosphorylated PMK-1 relative to total PMK-1 compared to
201 wild-type controls (Figs. 2E and 2F). In addition, RNAi-mediated knockdown of *tir-1*, the most
202 upstream component of the p38 signaling cassette [2, 3], fully suppressed hyperactivation of
203 T24B8.5p::*gfp* in *nhr-8(hd117)* animals (Fig. 2G). In addition, the *tir-1(qd4)* loss-of-function
204 mutation completely suppressed the induction of T24B8.5, *irg-4*, *irg-5*, and K08D8.4 in the *nhr-*
205 *8(hd117)* background (Figs. 2H-K). The transcription factors ATF-7 and SKN-1 link PMK-1 activity
206 to its transcriptional outputs [36, 37]. In *nhr-8(hd117)* animals, knockdown of *atf-7*, but not *skn-1,*
207 abrogated T24B8.5p::*gfp* activation (Figs. 2G and S2B). Finally, to further support our observation
208 that cholesterol scarcity induces immune defenses upstream of p38 PMK-1, we used the MAPK
209 phosphatase *vhp-1*, a negative regulator of PMK-1 [38]. Solubilization of cholesterol with Tergitol
210 was unable to suppress activation of T24B8.5p::*gfp* induced by knockdown of *vhp-1* (Fig. 2L).
211 Thus, the TIR-1-p38 PMK-1-ATF-7 signaling axis is activated in the *nhr-8* mutant background.

212 The c-JUN N-terminal kinase MAPK homolog *kgb-1*, the insulin signaling pathway
213 forkhead box O family (FOXO) transcription factor, *daf-16*, and the G protein-coupled receptor
214 (GPCR), *fshr-1*, each function in parallel to the p38 PMK-1 pathway to regulate immune and stress
215 responses in *C. elegans* [4, 38-40]. However, knockdown of each of these genes in *nhr-8(hd117)*
216 animals failed to suppress T24B8.5p::*gfp* activation (Fig. S2B) and RNAi-mediated knockdown of
217 *nhr-8* did not induce nuclear localization of DAF-16::GFP (Fig. S2C). Thus, cholesterol scarcity
218 induces *C. elegans* innate immune responses through specific activation of p38 PMK-1 immune
219 pathway signaling.
220
221 **Activation of the p38 PMK-1 pathway by cholesterol deprivation requires TIR-1**
222 **oligomerization and $NAD^+$ glycohydrolase activity.**
223 *C. elegans* TIR-1, which is homologous to mammalian SARM1, functions upstream of the
224 MAPKKK NSY-1; MAPKK SEK-1; MAPK p38 PMK-1 signaling cassette in the intestine to control
225 innate immune defenses [2, 41]. Accordingly, *tir-1* loss-of-function mutants are more susceptible
226 to killing by *P. aeruginosa* than wild-type animals [2]. The TIR-1 protein has three characterized
227 domains: a Heat/Armadillo repeat domain, a sterile alpha motif (SAM) domain, and a Toll-
228 interleukin receptor (TIR) domain [41] (Fig. 3A). *C. elegans* TIR-1 oligomerizes *in vitro* through
229 interactions of its SAM domains [42]. In addition, oligomerization of SARM1 is essential for its
230 function in plants and mice [42, 43]. As such, we evaluated whether the oligomerization of *C.*
231 *elegans* TIR-1 is required to activate the p38 PMK-1 immune pathway in the intestine. We used
232 CRISPR-Cas9 to delete both SAM domains in *tir-1* (*tir-1*$^{\Delta SAM}$) (Fig. 3A). We also generated point
233 mutants in two residues within the *C. elegans* TIR domain that are important for the self-
234 association and activity of mammalian SARM1 (*C. elegans tir-1*$^{G747P}$ and *tir-1*$^{H833A}$) [42] (Fig. 3A).
235 The *C. elegans tir-1*$^{\Delta SAM}$*, tir-1*$^{G747P}$ and *tir-1*$^{H833A}$ mutants prevented activation of the p38 PMK-1-
236 dependent immune reporter T24B8.5p::*gfp* in animals infected with *P. aeruginosa* (Fig. 3B), in
237 *nhr-8(RNAi)* animals (Fig. 3C), and during cholesterol deprivation (Fig. 3D). Consistent with these

238 data, the *tir-1*$^{\Delta SAM}$, *tir-1*$^{G747P}$ and *tir-1*$^{H833A}$ mutants have reduced levels of active, phosphorylated
239 p38 PMK-1, equivalent to the *tir-1(qd4)* null allele [32] (Figs. 3E and 3F). Additionally, these
240 mutants abrogate the induction of the T24B8.5 (Fig. 3G) and *irg-4* (Fig. S3A) immune effectors in
241 *nhr-8(RNAi)* animals and are each markedly hypersusceptible to *P. aeruginosa* infection (Fig. 3H).
242 The TIR domain of *C. elegans*, TIR-1, and its mammalian homolog, SARM1, possess
243 intrinsic NADase activity [42, 44, 45]. Importantly, oligomerization of mammalian SARM1 and *C.*
244 *elegans* TIR-1 is required for maximal NADase activity *in vitro* [42]. The NADase activity in the
245 TIR domain of mammalian SARM1 requires a putative catalytic glutamate [45]. We used CRISPR-
246 Cas9 to mutate the homologous glutamate in *C. elegans tir-1* (*tir-1*$^{E788A}$) and found that it was
247 required for the immunostimulatory activity of *tir-1* – *tir-1*$^{E788A}$ mutants do not induce T24B8.5p::*gfp*
248 following *P. aeruginosa* infection (Fig. 3B), knockdown of *nhr-8* (Fig. 3C) or during cholesterol
249 scarcity (Fig. 3D). Likewise, the *tir-1*$^{E788A}$ mutant animals had less active, phosphorylated p38
250 PMK-1 (Figs. 3E and 3F), completely suppressed the induction of T24B8.5 (Fig. 3G) and *irg-4*
251 (Fig. S3A) and were more susceptible to *P. aeruginosa* infection (Fig. 3H). We confirmed that *tir-*
252 *1*$^{E788A}$, *tir-1*$^{\Delta SAM}$, *tir-1*$^{G747P}$ and *tir-1*$^{H833A}$ mutants are translated and not degraded by introducing a
253 3xFLAG tag at the C-terminus of each mutant using CRISPR-Cas9 (Figs. S3B and S3C). A
254 western blot with an anti-FLAG antibody yielded a band of the expected size for each *tir-1* mutant
255 (Fig. S3B). In addition, the 3xFLAG-tagged wild-type TIR-1 expressed T24B8.5p::gfp normally,
256 but the tagged mutant TIR-1 proteins did not (Fig. S3C). Collectively, these data provide the first
257 genetic evidence that both the oligomerization of TIR-1 and its intrinsic NADase activity are
258 required to activate the p38 PMK-1 innate immune pathway.
259

260 **The NAD$^+$ glycohydrolase activity of TIR-1/SARM1 is activated by a phase transition**

261 To further characterize the mechanism of TIR-1/SARM1 activation, we recombinantly
262 expressed and purified the TIR domain of the TIR-1 protein (called TIR) from *E. coli* and evaluated

263 its NADase activity *in vitro* using an etheno-$NAD^+$ (ε-NAD) activity assay, in which hydrolysis of
264 the nicotinamide ring of ε-NAD leads to an increase in fluorescence. Interestingly, purified TIR
265 only shows very modest NADase activity even at high protein concentrations (>15 μM) (Fig. 4A).
266 Notably, the NADase activity of TIR increased parabolically with increasing TIR concentrations
267 rather than linearly, suggesting that multimerization of TIR-1 potentiates its NADase activity (Fig.
268 4A).

269 Given that high concentrations of TIR are required to observe NADase activity, we
270 hypothesized that molecular crowding might activate the enzyme and therefore assessed the
271 effect of several macro- and microviscogens on TIR activity. Macroviscogens reduce the free
272 volume available for protein movement and thus promote aggregation of protein complexes that
273 are capable of self-association [46, 47]. Importantly, macroviscogens have minimal impact on the
274 rate of diffusion of small molecules. By contrast, microviscogens, which are much smaller than
275 most enzymes, affect the diffusion of substrates in solution and thus, the frequency at which
276 enzymes encounter their substrate [47]. Interestingly, macroviscogens [polyethylene glycol (PEG)
277 3350 and PEG 8000], but not microviscogens (sucrose or glycerol), dramatically increased the
278 NADase activity of TIR (Fig. 4B). PEGs 3350 and 8000 increase TIR activity in a concentration-
279 dependent manner (Fig. 4C). These effects were most pronounced with higher molecular weight
280 PEGs, as treatment with smaller molecular weight PEGs (e.g., PEG 1500 and PEG 400) or
281 dextran did not increase the enzymatic activity of TIR (Fig. 4C). Crowding agents also increase
282 the activity of the TIR domain of human SARM1, as well as plant TIR domains [15, 42], suggesting
283 that the mechanism of TIR regulation is strongly conserved.

284 Treatment with macroviscogens enabled the characterization of the enzyme kinetics of
285 TIR. Incubation with 25% PEG 3350 led to a roughly linear association between TIR concentration
286 and NADase activity and markedly enhances TIR activity at each enzyme concentration (Fig.
287 S4A). Consequently, lower amounts of enzyme (2.5 μM TIR) can be used to obtain robust kinetic

288 data. Using these conditions, we determined the steady-state kinetic parameters ($k_{cat}$, $K_M$, and
289 $k_{cat}/K_M$) with 2.5 μM TIR in the presence of increasing concentrations of PEG 3350 (Fig. 4D). The
290 $K_m$ of TIR increases and then decreases to level off at ~500 μM of ε-NAD with increasing
291 concentration of PEG 3350 (Fig. 4E). On the other hand, $k_{cat}$ increases nearly linearly with
292 increasing concentrations of PEG 3350 (Fig. 4F). In addition, the catalytic efficiency ($k_{cat}/K_m$)
293 followed the same trend as $k_{cat}$, indicating that increased TIR activity is due to increased substrate
294 turnover by the enzyme and not tighter substrate binding (Fig. 4G).

295 We found that the NAD hydrolase activity of TIR is also activated by the precipitant sodium
296 citrate, providing an orthologous method to characterize the enzymatic activity of the TIR domain
297 (Figs. S4A and S4B). Notably, the response to increasing citrate concentration was switch-like,
298 where a concentration of at least 250 mM sodium citrate was needed to observe enzyme activity
299 (Figs. S4B and S4C). By contrast, activation with PEG 3350 was more dose-dependent (Figs. 4C
300 and 4D). Nevertheless, the kinetic parameters obtained in the presence of citrate displayed similar
301 trends to those found with PEG 3350: $K_m$ decreased to level off at ~400 μM of ε-NAD (Fig. S4D),
302 $k_{cat}$ increases with increasing sodium citrate concentration (Fig. S4E), and $k_{cat}/K_m$ follows the $k_{cat}$
303 trends (Fig. S4F).

304 In the cytoplasm, high concentrations of macromolecules (proteins, nucleic acids, lipids,
305 carbohydrates) cause molecular crowding and induce phase transitions of signaling proteins [48].
306 To determine if TIR undergoes a phase transition and whether its NADase activity correlates with
307 the transition, we incubated purified TIR with different concentrations of PEG3350 or citrate,
308 centrifuged the sample, and evaluated TIR NADase activity in the soluble and insoluble fractions
309 (Figs. 4H and S4G). At low concentrations of both PEG and citrate, TIR protein was present in
310 the supernatant. However, at high concentrations of both PEG and citrate, TIR was principally
311 located in the pelleted (insoluble) fraction, as visualized by Coomassie staining on an SDS-PAGE
312 gel (Figs. 4H and S4G). Importantly, robust NADase activity was observed in the pelleted fraction,

313 and not in the supernatant of samples treated with high concentrations of PEG or citrate (Figs.
314 4H and S4G). Taken together, these data demonstrate that precipitation/aggregation of TIR is
315 required to activate the intrinsic NADase activity of TIR-1/SARM1.

316

317 **TIR phase transition and $NAD^+$ glycohydrolase activity requires TIR oligomerization.**

318 To determine whether TIR-1 oligomerization is also required for a phase transition and the
319 NADase activity of TIR, we recombinantly expressed and purified the TIR domain of TIR-1, which
320 contained mutations in residues required for oligomerization ($TIR^{G747P}$ and $TIR^{H833A}$) and $NAD^+$
321 hydrolysis ($TIR^{E788A}$ and $TIR^{E788Q}$). Notably, $TIR^{G747P}$ and $TIR^{E788Q}$ mutants showed no apparent
322 activity and $TIR^{E788A}$ and $TIR^{H833A}$ showed a $>1x10^8$-fold decrease in catalytic efficiency ($k_{cat}/K_m$)
323 compared to $TIR^{WT}$ (Fig. 4I). Similarly, kinetic analysis of TIR oligomerization and catalytic
324 mutants in 500 mM citrate revealed that all the mutants were catalytically dead, each showing no
325 apparent activity (Fig. S4H).

326 To further characterize the TIR phase transition, we evaluated the precipitation capacity
327 of TIR oligomerization and catalytic mutants in the presence of PEG 3350 and citrate. Consistent
328 with our genetic data, $TIR^{G747P}$, which contains a mutation that prevents oligomerization of TIR,
329 was unable to precipitate as readily as $TIR^{WT}$ (Fig. 4J). Compared to $TIR^{WT}$, the $TIR^{G747P}$ mutant
330 in the presence of PEG 3550 demonstrated a 25% decrease in the amount of precipitated protein
331 (Fig. 4J). We observed similar results in the presence of citrate, in which compared to $TIR^{WT}$, the
332 $TIR^{G747P}$ mutant demonstrated a 22% decrease in precipitated protein compared to $TIR^{WT}$ (Fig.
333 S4I). Importantly, TIR proteins with two different mutations in the glutamate required for $NAD^+$
334 catalysis, $TIR^{E788A}$ and $TIR^{E788Q}$, precipitated to a similar extent as $TIR^{WT}$ (Figs. 4J, 4K, S4I, and
335 S4J), but had minimal NADase activity (Figs. 4I and S4H). Collectively, these data demonstrate
336 that a phase transition of TIR-1 is required for its NADase activity.

337

338 **A phase transition superactivates the intrinsic $NAD^+$ glycohydrolase activity of TIR.**

339 During phase separations, macromolecules partition into distinct biochemical
340 compartments characterized by a higher concentration dense phase and a lower concentration
341 dilute phase [10, 11, 13]. The dense compartment can have either liquid-like properties in liquid-
342 to-liquid phase separations or solid-like properties in liquid-to-solid phase transitions [11, 12, 14,
343 49]. To determine whether TIR undergoes a liquid-to-liquid or a liquid-to-solid phase transition,
344 we assayed the enzyme activity of TIR in the presence of 1,6-hexanediol, an aliphatic alcohol that
345 interferes with hydrophobic interactions prominent in liquid-to-liquid separations. Thus, 1,6-
346 hexanediol disrupts liquid-like compartments, but not solid-like compartments [10, 13, 14]. In the
347 presence of either PEG 3350 or citrate, we observed that 1,6-hexanediol decreases the NADase
348 activity of TIR by <2-fold, yet the activity of 1,6-hexanediol-treated TIR remains two orders of
349 magnitude higher than the activity of TIR without PEG 3550 or citrate addition (Fig. 5A). While
350 significant, this modest effect suggests that the NADase activity of TIR is predominantly
351 associated with a solid, rather than a liquid, state (Fig. 5A). Notably, in the absence of PEG 3350
352 or citrate, the low-level TIR NADase activity can be inhibited by 1,6-hexanediol (Fig. 5A),
353 suggesting that this activity is driven by hydrophobic interactions. Importantly, 1,6-hexanediol
354 does not interfere with TIR precipitation in the presence of PEG or citrate, regardless of whether
355 it is added before or after precipitate formation (Figs. S5A and S5B).

356 Next, we determined if this liquid-to-solid phase transition of TIR is reversible. The
357 insoluble fraction following treatment of TIR with PEG 3350 or citrate was resuspended in either
358 buffer alone or buffer plus the respective additive (PEG 3350 or citrate). If the phase transition is
359 reversible, resuspension of precipitated TIR in buffer alone should disrupt enzymatic activity.
360 However, if the phase transition is irreversible, activity should be detected when the pellet is
361 resuspended in buffer alone. Notably, we observed some TIR enzymatic activity when the pellet
362 was resuspended in buffer (Fig. 5B). With PEG 3350, the activity was lower than that observed in

363 the pre-centrifugation control or when the pellet was resuspended in buffer with PEG 3350. By
364 contrast, with citrate, the activity was similar to both control conditions (pre-centrifugation or when
365 the pellet was resuspended in buffer and citrate). These data indicate that the phase transition of
366 TIR is partially reversible in PEG 3350 and irreversible in sodium citrate. To confirm these findings,
367 we centrifuged the resuspended samples to examine the fractions visually by SDS-PAGE. In the
368 sample initially prepared with PEG 3350 and resuspended in buffer alone, a faint band was
369 present in the supernatant fraction. However, this band was absent in the sample initially prepared
370 with sodium citrate (Fig. 5C). These data confirm that the TIR phase transition is partially
371 reversible in PEG 3350 and irreversible in sodium citrate, at least under these conditions.

372 Next, we evaluated the effect of pH on TIR precipitation and NADase activity. There was
373 virtually no increase in TIR precipitation in the absence of PEG. However, in the presence of 25%
374 PEG, TIR precipitation increased with increasing pH (Fig. 5D). Under these same conditions, no
375 activity was apparent below pH 6. $K_m$ remained constant (Fig. 5E) and $k_{cat}$ increased from pH 6.5
376 to pH 8.5 (Fig. 5F). A corresponding increase in $k_{cat}/K_m$ was responsible for the increase in
377 catalytic efficiency above pH 7 (Fig. 5G). Notably, the increase in $k_{cat}/K_m$ correlated with
378 precipitation (Figs. 5D and 5G), again indicating that a phase transition increases TIR activity.

379 We performed negative stain electron microscopy to directly visualize TIR aggregation *in*
380 *vitro*. Protein visualization is not possible with PEG because macroviscogens themselves are
381 stained, confounding image analysis. Therefore, we performed this experiment with citrate. In the
382 absence of citrate, we observed borderline fibrillar structures and protein aggregates, but overall,
383 there were no consistent structures (Fig. 5H). However, in the presence of citrate, circular particles
384 emerged (Fig. 5H). These results indicate that, *in vitro*, TIR aggregates into higher-order, ring-like
385 structures.

386

387 **Physiologic stresses, both pathogen and non-pathogen, induce multimerization of TIR-**
388 **1/SARM1 into visible puncta within intestinal epithelial cells.**

389 To visualize TIR-1 aggregation *in vivo*, we used CRISPR/Cas9 to insert wrmScarlet at the
390 C-terminus of the endogenous *C. elegans tir-1* locus, which labeled all *tir-1* isoforms. In uninfected
391 animals, TIR-1::wrmScarlet is barely detectable in intestinal epithelial cells (Fig. 6A). However, *P.*
392 *aeruginosa* infection caused TIR-1::wrmScarlet to multimerize into visible puncta within intestinal
393 epithelial cells (Fig. 6A and 6B). We distinguished TIR-1::wrmScarlet puncta from autofluorescent
394 gut granules by comparing images in the red and green fluorescence channels. TIR-1::wrmScarlet
395 puncta are those that are seen in the red, but not the green fluorescence channel (arrowhead in
396 Fig. 6), as opposed to gut granules, which can be seen in both channels (asterisks in Fig. 6).
397 Importantly, *tir-1(RNAi)* ablated TIR-1::wrmScarlet formation in the red fluorescence channel, but
398 did not affect gut granule auto-fluorescence (Fig. 6A and 6B).

399 Sterol depletion in *nhr-8(hd117)* animals also induced TIR-1::wrmScarlet puncta formation
400 in intestinal epithelial cells (Fig. 6C and 6D). Importantly, TIR-1::wrmScarlet puncta formation in
401 *nhr-8(hd117)* animals was entirely suppressed by solubilizing cholesterol in the growth media with
402 Tergitol (Fig. 6C and 6D). Additionally, treatment of *nhr-8(hd117)* animals expressing TIR-
403 1::wrmScarlet with *tir-1(RNAi)* inhibited fluorescence and puncta formation (Fig. 6C and 6D).

404 Taken together, these data demonstrate for the first time that physiological stressors, both
405 pathogen and non-pathogen, induce TIR-1 multimerization into puncta within intestinal epithelial
406 cells, which superactivates the intrinsic NADase activity of this protein complex to activate the
407 p38 PMK-1 innate immune pathway.

408

409 **Sterol scarcity primes p38 PMK-1 immune defenses.**

410 Since *C. elegans* require cholesterol to survive bacterial infection and must obtain this
411 essential metabolite from their diet, we hypothesized that, when environmental sterols are limited,
412 activation of the p38 PMK-1 pathway represents an evolutionary adaptation that primes immune
413 effector expression to anticipate challenges from bacterial pathogens. To test this hypothesis, we

414 examined the expression of innate immune effector genes during bacterial infection in the
415 presence and absence of cholesterol supplementation. Interestingly, the induction of *irg-4*p::*gfp*
416 (Fig. 7A), *irg-5*p::*gfp* (Fig. 7B) and T24B8.5p::*gfp* (Fig. 7C) during *P. aeruginosa* infection was
417 enhanced when nematodes were infected on media that did not contain supplemented
418 cholesterol. Consistent with these data, *P. aeruginosa* infection also led to increased activation of
419 *irg-4*p::*gfp* (Fig. 7D) and *irg-5*p::gfp (Fig. 7E) when *nhr-8* was depleted by RNAi. These data
420 suggest that cholesterol scarcity primes p38 PMK-1 immune defenses for subsequent pathogen
421 encounter.

422 To provide further support for this hypothesis, we analyzed the expression pattern of p38
423 PMK-1-dependent transcripts in *nhr-8(hd117)* mutant animals during *P. aeruginosa* infection. Of
424 the 472 genes that were induced in wild-type animals during *P. aeruginosa* infection, 184 were
425 also differentially regulated (either induced or repressed) in *nhr-8(hd117)* animals that were
426 infected with *P. aeruginosa*. To perform this analysis in an unbiased manner, we scaled the
427 expression level in each condition for each of these 184 genes by calculating a row z-score and
428 performed hierarchical clustering (Fig. 7F). We observed that these 184 genes group into two
429 clusters: Cluster I had 139 genes and Cluster II contained 45 genes (Table S3). Cluster I was
430 comprised mostly of genes whose expression in the absence of infection was higher in *nhr-*
431 *8(hd117)* mutants than wild-type animals (129 of 139 genes). In addition, the majority of Cluster I
432 genes were more strongly induced during *P. aeruginosa* infection in *nhr-8(hd117)* animals than
433 wild-type animals. Cluster II, on the other hand, contained genes whose induction on *P.*
434 *aeruginosa* were dependent on *nhr-8*. Interestingly, p38 PMK-1-dependent genes were strongly
435 enriched among Cluster I, but not Cluster II, genes (Fig. 7G). Thirty-three of the 139 genes in
436 Cluster I are known targets of the p38 PMK-1 immune pathway (24.17-fold enriched,
437 hypergeometric p-value = $7.68 \times 10^{-37}$), a group that includes the immune effectors T24B8.5 (Fig.
438 7H), *irg-4* (Fig. 7I), *irg-5* (Fig. 7J) and K08D8.4 (Fig. 7K). By contrast, only three genes in Cluster

439 II are p38 PMK-1 dependent transcripts (6.95-fold enriched, hypergeometric p-value = 0.01) (Figs.
440 7F and 7G).

441 These data demonstrate that sterol scarcity primes the induction of innate immune
442 effectors by activating the p38 PMK-1 immune pathway. Subsequent challenge by *P. aeruginosa*
443 further drives immune activation in a manner that promotes clearance of pathogenic bacteria from
444 the intestine (Fig. 1O).

445 **DISCUSSION**

446 In this manuscript, we report two conceptual advances. First, we show that a phase
447 transition of *C. elegans* TIR-1, an $NAD^+$ glycohydrolase homologous to mammalian SARM1,
448 underlies p38 PMK-1 immune pathway activation in the *C. elegans* intestine (Fig. 7L).
449 Importantly, we demonstrate that physiologic stresses, both pathogen and non-pathogen, induce
450 multimerization of TIR-1/SARM1 into visible puncta within intestinal epithelial cells. *In vitro*
451 biochemical studies of purified protein and *C. elegans* genetic analysis revealed that
452 multimerization and a phase transition of TIR-1/SARM1 engages its $NAD^+$ glycohydrolase activity
453 to activate the p38 PMK-1 innate immune pathway and provide protection during bacterial
454 infection.

455 Second, we show that the TIR-1/SARM1 phase transition is modified by dietary
456 cholesterol, revealing a new adaptive response that allows a metazoan host to anticipate
457 environmental threats during micronutrient deprivation, a time of relative susceptibility to infection.
458 *C. elegans* lack the ability to synthesize cholesterol *de novo* and must acquire dietary sterols from
459 its environment to support development, fecundity, lifespan, and resistance against pathogen
460 infection [19-25]. *C. elegans* larvae that encounter sterol-scarce environments are primed to enter
461 an alternative developmental program, called dauer diapause, which promotes animal survival, in
462 part, by altering their metabolism and growth to conserve energy [26-30]. Interestingly, only a
463 fraction of sterol-starved *C. elegans* larvae enter dauer diapause and the remaining animals
464 develop to adulthood [28, 34]. Here, we show that cholesterol starvation promotes multimerization
465 of TIR-1/SARM1 into puncta, which activates the p38 PMK-1 immune pathway. Importantly,
466 anticipatory activation of innate immune defenses in this manner during conditions of low
467 cholesterol availability augments immune effector induction and promotes pathogen clearance
468 from the intestine during a subsequent bacterial infection.

469 It is important to note that the conclusion of our manuscript regarding the role of cholesterol
470 in *C. elegans* pathogen resistance is fundamentally different from the findings of Otarigho et al.

471 [24]. These authors found that supraphysiologic concentrations of cholesterol given in the
472 absence of infection drove the activation of immune effector genes in an RNA-seq experiment,
473 five of which were dependent on *nhr-8* for their induction in this context using qRT-PCR. Together
474 with genetic studies during pathogen infection, the authors conclude that NHR-8 controls immune
475 genes downstream of multiple *C. elegans* pathways, including the p38 PMK-1 pathway. Indeed,
476 in our genome-wide transcriptome profiling experiment, we observed that a small number of
477 genes required *nhr-8* for their full induction during *P. aeruginosa* infection (Class II genes, Fig.
478 7F), a group that includes some genes downstream of the p38 PMK-1 pathway (Fig. 7G).
479 However, we discovered that neither immune effectors, nor p38 PMK-1 targets, were enriched
480 among the genes that were transcriptionally repressed upon exposure to 0 mg/ml cholesterol or
481 in two *nhr-8* loss-of-function mutants (Figs. 1D, 1E, 2A, 2D, S1A and S2A). Rather, genes
482 dependent on p38 PMK-1 for their transcription were strongly activated during cholesterol
483 deprivation (both in wild-type animals exposed to 0 mg/mL cholesterol and in two *nhr-8* mutants
484 at baseline, both in the absence of infection) (Figs. 1D, 1E, 2A, 2D, S1A and S2A). In addition,
485 the induction of these p38 PMK-1-dependent immune effectors were strongly augmented during
486 pathogen infection (Class I genes, Figs. 7F and 7G). We confirmed in western blot experiments
487 and genetic epistasis analyses that the p38 PMK-1 pathway is activated in multiple *nhr-8* loss-of-
488 function mutants and in wild-type animals grown in the absence of exogenous cholesterol (Fig.
489 2). We also employed two orthologous assays to demonstrate that the hypersusceptibility of
490 multiple *nhr-8* mutants to *P. aeruginosa* infection is due to sterol deficiency in these animals (Figs.
491 1M and 1N). Finally, we show that low cholesterol in *nhr-8* mutants leads to markedly enhanced
492 induction of p38 PMK-1-dependent immune effector expression during *P. aeruginosa* infection
493 (Class I genes, Fig. 7F) in a manner that promotes clearance of pathogen from the intestine (Fig.
494 1O). Thus, our study reveals that cholesterol deficiency primes protective activation of the p38
495 PMK-1 immune pathway in the *C. elegans* intestine.

496 We previously demonstrated that a *C. elegans* nuclear hormone receptor, NHR-86, a
497 member of a family of ligand-gated transcription factors, surveys the chemical environment to
498 activate the expression of immune effectors [50]. Interestingly, NHR-86 targets immune effectors
499 whose basal regulation requires the p38 PMK-1 immune pathway. However, NHR-86 functions
500 independently of PMK-1 and modulates the transcription of these infection response genes
501 directly. NHR-86 is a nematode homolog of the mammalian nuclear hormone receptor hepatocyte
502 nuclear factor 4 (HNF4), a family of NHRs that expanded dramatically in *C. elegans* (259 HNF4
503 homologs are encoded in the *C. elegans* genome) [51, 52]. One potentially unifying hypothesis is
504 that HNF4 homologs detect pathogen- or host-derived ligands that are associated with infection
505 and activate pathogen-specific immune defenses. In this model, the p38 PMK-1 pathway
506 functions as a rheostat that receives inputs from signals associated with potentially dangerous
507 environmental conditions to prime host immune effector genes. Indeed, inputs from
508 chemosensory neurons, bacterial density, tissue damage and nucleotide metabolism also
509 regulate the tonic level of p38 PMK-1 pathway activity [3, 53-57], suggesting that p38 PMK-1
510 phosphorylation is adjusted to anticipate dangerous threats during periods of vulnerability. Thus,
511 upon encountering a pathogen, immune defenses can be further augmented by other
512 mechanisms that detect pathogen specifically.

513 SARM1, the mammalian homolog of TIR-1, has a well-characterized role in promoting
514 Wallerian degeneration, a form of neuronal degeneration induced by axon injury [58, 59]. In *in*
515 *vitro* models of axon injury, SARM1 NADase activity depletes $NAD^+$ and induces axonal death
516 [58]. Loring et al. reported that a phase transition of mammalian SARM1 potentiates its intrinsic
517 NADase activity, as we observed for *C. elegans* TIR-1 [15]. These authors found that treatment
518 with high concentrations of citrate, a precipitant that induces protein aggregation, caused *C.*
519 *elegans* TIR-1/SARM1 to form puncta in neurons. Exposure of *C. elegans* to citrate was also
520 correlated with enhanced axonal degeneration. Citrate exposure in this experiment does not
521 represent a physiologically relevant stress, however. Thus, the findings reported here that TIR-

522 1/SARM1 oligomerizes in response to a pathogen and non-pathogen stress provides an important
523 characterization of the mechanism inferred by Loring, et al, and demonstrates that this
524 phenomenon occurs in non-neuronal tissues in the regulation of intestinal immunity. Interestingly,
525 the enzyme kinetics of TIR-1 are strikingly similar to mammalian SARM1 – the activity of both
526 proteins is exquisitely dependent on precipitation. Thus, the mechanism of TIR-1/SARM1
527 activation is conserved across millions of years of evolution, functions in different cellular contexts,
528 and underlies both axonal degeneration following neuronal injury and the regulation of the p38
529 PMK-1 pathway activation in the control of intestinal immunity.

**ACKNOWLEDGEMENTS AND FUNDING SOURCES**

The authors thank Alexandra Byrne, Victoria Czech, Lauren O'Connor, and Heather Loring for helpful discussions. The authors are also grateful to Melanie Trombly and Merin MacDonald for critical reading of the manuscript. This research was supported by R01 AI130289 (to R.P.W.), R21 AI163430 (to R.P.W.), an Innovator Award from the Kenneth Rainin Foundation (to R.P.W.), the Dan and Diane Riccio Fund for Neuroscience (to R.P.W. and P.R.T.), F30 AI150127 (to N.D.P.), T32 AI132152 (to N.D.P. and J.D.I.), T32 GM107000 (to N.D.P.), and R35 GM118112 (to P.R.T.). Some strains were provided by the *Caenorhabditis* Genetics Center, which is funded by the NIH Office of Research Infrastructure Programs (P40 OD010440).

539 **MATERIALS AND METHODS**

540 ***C. elegans* and bacterial strains.** The previously published *C. elegans* strains used in this
541 study were: N2 Bristol [31], KU25 *pmk-1(km25)* [60], AU3 *nsy-1(ag3)* [1], ZD101 *tir-1(qd4)* [32],
542 AA968 *nhr-8(hd117)* [34], AE501 *nhr-8(ok186)* [35], AU78 *agIs219* [T24B8.5p::*gfp*::*unc-54-*
543 3'UTR; *ttx-3*p::*gfp*::*unc-54*-3'UTR] [32], AU306 *agIs44* [*irg-4*p::*gfp*::*unc-54*-3'UTR*; myo-*
544 *2*p::*mCherry*] [61], AY101 *acIs101* [p*DB09.1(irg-5*p::*gfp)*; pRF4(*rol-6(su1006)*)] [33], TJ356
545 *zIs356* [*daf-16*p::*daf-16a/b*::*gfp* + pRF4(*rol-6(su1006)*)], *MGH167 sid-1(qt9); alxIs9[vha-6p::sid-*
546 *1::SL2::GFP]*. The strains developed in this study were: RPW278 *nhr-8(hd117)*;*agIs219*,
547 RPW317 *tir-1(qd4)*;*nhr-8(hd117)*, RPW339 *tir-1(ums47[E788A])*;*agIs219*, RPW369 *tir-*
548 *1(ums54[ΔSAM])*;*agIs219*, RPW374 *tir-1(ums55[G747P])*;*agIs219*, RPW381 *tir-*
549 *1(ums56[H833A])*;*agIs219*, RPW386 *tir-1(ums57[tir-1::3xFLAG])*;*agIs219*, RPW387 *tir-*
550 *1(ums58[tir-1[E788A]::3xFLAG])*;*agIs219*, RPW388 *tir-1 (ums59[tir-*
551 *1[ΔSAM]::3xFLAG])*;*agIs219*, RPW 389 *tir-1(ums60[tir-1[G747P]::3xFLAG])*;*agIs219*, RPW403
552 *tir-1(ums63[tir-1::wrmScarlet])*, RPW404 *nhr-8(hd117)*;*tir-1(ums63[tir-1::wrmScarlet])*. Bacteria
553 used in this study are *Escherichia coli* OP50, *E. coli* DH5α, *E. coli* HT115(DE3), and
554 *Pseudomonas aeruginosa* strain PA14 [62].

555

556 ***C. elegans* growth conditions and lipid supplementation.** *C. elegans* strains were maintained
557 on standard nematode growth medium (NGM) plates [0.25% bacto peptone, 0.3% sodium
558 chloride, 1.7% agar (Fisher), 5 µg/mL cholesterol (Sigma-Aldrich, BioReagent grade), 25 mM
559 potassium phosphate pH 6.0, 1 mM magnesium sulfate, 1 mM calcium chloride] with *E. coli* OP50
560 as a food source, as described [31]. For low cholesterol medium (0 µg/mL cholesterol), NGM was
561 prepared without cholesterol supplementation, while 0.1% ethanol was added to maintain an
562 equivalent ethanol concentration. For high cholesterol medium, cholesterol was dissolved in
563 ethanol at 20 mg/mL and added to NGM at a final concentration of 80 µg/mL immediately prior to
564 pouring plates. For all assays with high cholesterol medium, NGM containing 0.4% ethanol and 5

565 µg/mL cholesterol were used as control plates. Cholesterol solubilization assays were performed
566 by supplementing NGM containing 5 µg/mL cholesterol with either 0.1% Tergitol (Sigma-Aldrich)
567 or 0.1% Triton X-100 (Sigma-Aldrich). For assays using media solidified with agarose, NGM
568 plates were prepared with 1.7% Ultrapure agarose (ThermoFisher Scientific) in place of agar. All
569 fatty acids were purchased from Nu-Check-Prep Inc. and supplementation performed as
570 previously described with modification [63, 64]. Fatty acids were dissolved in 50% ethanol and
571 added at a final concentration of 1 mM to NGM agarose containing 0 µg/mL cholesterol and 0.1%
572 Tergitol immediately prior to plate pouring. Prior to all assays, plates supplemented with lipids and
573 control plates were seeded with *E. coli* OP50 and grown for 24 hours at room temperature. Assays
574 were performed by picking 10-20 gravid adult animals to either lipid-supplemented or matched
575 control plates. Animals were maintained on the plates for 14 hours at 20ºC after which they were
576 removed. Eggs laid on the plate were allowed to hatch and develop to the L4 stage at 20ºC. For
577 low cholesterol assays, animals were grown for two generations on NGM containing 0 µg/mL
578 cholesterol.
579
580 ***C. elegans* strain construction**. CRISPR/Cas9 was used to generate *tir-1* mutants in both wild-
581 type and TIR-1::3xFLAG backgrounds, as described [65, 66]. All CRISPR/Cas9 reagents were
582 purchased from Integrated DNA Technologies. Target guide sequences were selected using the
583 CHOPCHOP web tool [67]. ssODN and dsDNA repair templates contained indicated edits,
584 deletions or insertions with 35 bp flanking homology arms. crRNA guide and ssODN sequences
585 are listed in Table S4. For wrmScarlet dsDNA repair template, wrmScarlet was PCR amplified
586 with 35 bp flanking homology arms. PCR was gel purified, diluted to 100 ng/µL, melted and
587 reannealed using a thermal cycler (95 ºC - 2 minutes; 85 ºC – 10 seconds, 75 ºC – 10 seconds,
588 65 ºC – 10 seconds, 55 ºC – 10 seconds, 45 ºC – 10 seconds, 35 ºC – 10 seconds, 25 ºC – 10
589 seconds, 4 ºC – hold. Ramp down 1 ºC per second), and used immediately for injection. A mixture
590 of 0.25 µg/µL Cas9, 0.1 µg/µL tracrRNA and 0.056 µg/µL crRNA were incubated for 15 minutes

591 at 37ºC. 0.11 µg/µL ssODN or 25 ng/µL dsDNA and 40 ng/µL pRF4(*rol-6(su1006)*) plasmid were
592 added to the mixture, centrifuged and microinjected into young adult animals carrying the *agIs219*
593 transgene, *tir-1(ums57[tir-1::3xFLAG])*;*agIs219*, or N2. The F1 progeny were screened for Rol
594 phenotypes 3-4 days after injection and then for indicated edits using PCR and Sanger
595 sequencing. Primer sequences used for genotyping are listed in Table S4.
596
597 **Feeding RNAi.** Knockdown of target genes was performed by feeding *C. elegans E. coli* HT115
598 expressing dsRNA targeting the gene of interest, as previously described with modification [68-
599 70]. In brief, HT115 bacteria expressing dsRNA targeting genes of interest were grown in
600 Lysogeny broth (LB) Lennox medium containing 50 µg/mL ampicillin and 15 µg/mL tetracycline
601 overnight with shaking (250 rpm) at 37ºC. Overnight cultures were seeded onto NGM containing
602 5 mM IPTG and 50 µg/mL carbenicillin and incubated at 37ºC for 16 hours after which
603 synchronized L1 animals were transferred to bacterial lawns and allowed to grow until the L4
604 stage.
605
606 ***C. elegans* Bacterial Infection and Colonization Assays.** "Slow killing" *P. aeruginosa* infection
607 experiments were performed as previously described [71, 72]. Wild-type is either N2 or *agIs219*.
608 In brief, a single colony of *P. aeruginosa* PA14 was inoculated into 3-mL of LB medium and grown
609 with shaking (250 rpm) at 37ºC for 14 hours. 10-µL of overnight culture was spread onto 35-mm
610 petri dishes containing 4-mL slow killing agar (0.35% peptone, 0.3% sodium chloride, 1.7% agar,
611 5 µg/mL cholesterol, 25 mM potassium phosphate pH 6.0, 1 mM magnesium sulfate, 1 mM
612 calcium chloride). Plates were incubated for 24 hours at 37ºC and for approximately 24 hours at
613 25ºC. Immediately prior to starting the assay 0.1 mg/mL 5-fluorodeoxyuridine (FUDR) was added
614 on top of the agar to prevent progeny from hatching. Animals used in all assays were grown at
615 20ºC with specified growth conditions. For assays involving high cholesterol or nonionic
616 detergents, slow killing agar plates were prepared with either 80 µg/mL cholesterol (Sigma-

617 Aldrich), 0.1% Tergitol (Sigma-Aldrich), or 0.1% Triton X-100 (Sigma-Aldrich). For experiments
618 using plates containing 80 µg/mL cholesterol, matched control plates containing the equivalent
619 ethanol concentration (0.4%) and 5 µg/mL cholesterol were prepared. All pathogenesis and
620 lifespan assays are representative of three biological replicates. Sample sizes, mean lifespan,
621 and p values for all trials are shown in Table S2.

622 Colony forming units of *P. aeruginosa* were quantified in the intestine of *C. elegans* as
623 previously described with modifications [72, 73]. Briefly, *C. elegans* animals were exposed to
624 lawns of *P. aeruginosa*, which were prepared as previously described, for 24 hours. Animals were
625 then picked to NGM plates lacking bacteria and incubated for 10 minutes to remove external *P.*
626 *aeruginosa*. Animals were then transferred to a second NGM plate after which 10-11 animals per
627 replicate were collected, washed with M9 buffer containing 25 mM tetramisole (Sigma-Aldrich)
628 and 0.01% Triton X-100 (Sigma-Aldrich), and ground with 1.0 mm silicon carbide beads (BioSpec
629 Products). *P. aeruginosa* CFUs were quantified from serial dilutions of the lysate grown on LB
630 agar.

631

632 **Gene expression analysis and bioinformatics.** 2,000 synchronized L1 stage *C. elegans* of the
633 indicated genotypes were grown to the L4 stage and harvested by washing with M9. For
634 expression analysis of *C. elegans* genes during *P. aeruginosa* infection, animals at the L4 stage
635 animals were transferred by washing to plates containing *E. coli* OP50 or *P. aeruginosa* PA14
636 lawns. Animals were exposed for four hours and subsequently harvested by washing with M9.
637 RNA was isolated using TriReagent (Sigma-Aldrich), column purified (Qiagen), and analyzed by
638 100 bp paired-end mRNA-sequencing using the BGISEQ-500 platform (BGIAmericasCorp) with
639 >20 million reads per sample. Raw fastq reads were evaluated by FastQC (version 0.11.5), clean
640 reads were aligned to the *C. elegans* reference genome (WBcel235) and quantified using Kallisto
641 (version 0.45.0) [74]. Differentially expressed genes were identified using Sleuth (version 0.30.0)
642 [75]. For identification of differentially expressed genes from animals grown in the absence (0

643 µg/mL) versus presence (5 µg/mL) of cholesterol supplementation, we analyzed previously
644 generated publicly available RNA-seq data from Otarigho et al. [24] using eVITTA [76]. Pearson
645 correlation statistical analysis was performed using Prism 9.0. Innate immune genes were
646 identified using DAVID Bioinformatics database biological process gene ontology (GO) term
647 innate immune response [77]. Heat-maps of differentially expressed genes were generated using
648 pheatmap (version 1.0.12). Gene set enrichment analysis of RNA-seq was performed using
649 GSEA (version 4.1.0) [78] with a custom gene set database containing p38 PMK-1 dependent
650 genes generated from previously published RNA-seq of uninfected *pmk-1(km25)* animals [79].
651 Differential gene expression was defined as a fold change (FC) versus wild-type greater than 2
652 and q less than 0.01.

653 For the qRT-PCR studies, RNA was reverse transcribed to cDNA using the iScript™ cDNA
654 Synthesis Kit (Bio-Rad Laboratories, Inc.), amplified and detected using Syber Green (Bio-Rad
655 Laboratories, Inc.) and a CFX384 machine (Bio-Rad Laboratories, Inc.). The sequences of
656 primers that were designed for this study are presented in Table S4. Other primers were
657 previously published [4, 80-82]. All values were normalized against the geometric mean of the
658 control genes *snb-1* and *act-3*. Fold change was calculated using the Pfaffl method [83].

659

660 **Immunoblot analyses.** Protein lysates from 2,000 *C. elegans* grown to the L4 larval stage on *E.*
661 *coli* OP50 on NGM agar were prepared as previously described with modification [50, 84].
662 Harvested animals were washed twice with M9 buffer and resuspended in RIPA Buffer (Cell
663 Signaling Technology, Inc.) containing 1x Halt Protease and Phosphatase inhibitor
664 (ThermoFisher Scientific). Samples were lysed using a teflon homogenizer, centrifuged, and
665 protein was quantified from the supernatant of each sample using the DC protein assay (Bio-Rad
666 Laboratories, Inc.). NuPAGE™ LDS sample buffer (ThermoFisher Scientific) was added to a
667 concentration of 1X and 12.5-30 µg of total protein from each sample was resolved on NuPAGE™
668 4-12% BisTris (Phospho-PMK-1 and Total-PMK-1) or NuPAGE™ 3-8% TrisAcetate (TIR-

669 1::3xFLAG) gels (ThermoFisher Scientific), transferred to nitrocellulose membranes using a
670 Trans-Blot Turbo Transfer System (Bio-Rad Laboratories, Inc.), blocked with 5% milk powder in
671 TBST and probed with a 1:1000 dilution of an antibody that recognizes the doubly-phosphorylated
672 TGY motif of PMK-1 (Cell Signaling Technology, #9211), a previously characterized total PMK-1
673 antibody [50], a monoclonal mouse anti-FLAG antibody (Sigma-Aldrich, M2), or a monoclonal
674 mouse anti-tubulin antibody (Sigma-Aldrich, Clone B-5-1-2). Horseradish peroxidase (HRP)-
675 conjugated anti-rabbit (Cell Signaling Technology, #7074) and anti-mouse IgG secondary
676 antibodies (Abcam, #ab6789) were diluted 1:10,000 and used to detect the primary antibodies
677 following the addition of ECL reagents (Thermo Fisher Scientific, Inc.), which were visualized
678 using a BioRad ChemiDoc MP Imaging System. The band intensities were quantified using
679 ImageJ version 2.0.0, and the ratio of active phosphorylated PMK-1 to total PMK-1 was
680 calculated.
681
682 **TIR-1::wrmScarlet puncta visualization and quantification.** For TIR-1::wrmScarlet puncta
683 visualization, all TIR-1::wrmScarlet expressing animals were depleted of autofluorescent gut
684 granules by exposure to *glo-3(RNAi)* from the L1 stage prior to all experiments. *P. aeruginosa*
685 was prepared as described for bacterial infection and colonization assays. L4 animals expressing
686 TIR-1::wrmScarlet were transferred to either OP50 or *P. aeruginosa* containing plates for 24
687 hours. For imaging, animals were transferred to 2% agarose pads, paralyzed with 300 mM sodium
688 azide, and imaged with a 63x oil immersion lens. For Tergitol experiments, animals were grown
689 on RNAi plates containing 0.1% Tergitol and the respective RNAi strains and imaged at the L4
690 stage. Image processing and analysis was performed using Fiji image analysis software. In each
691 panel, the exposure time and processing for all images were identical. To quantify TIR-
692 1::wrmScarlet puncta, maximum pixel intensity in the last posterior pair of intestinal epithelial cells
693 in both the red (TIR-1::wrmScarlet) and green (autofluorescence) channels were quantified.
694

695 **Microscopy.** Nematodes were mounted onto agar pads, paralyzed with 10 mM levamisole
696 (Sigma) or 300 mM sodium azide and photographed using a Zeiss AXIO Imager Z2 microscope
697 with a Zeiss Axiocam 506mono camera and Zen 2.3 (Zeiss) software.
698
699 **TIR-1 TIR domain expression and purification.** The recombinant *C. elegans* TIR-1 TIR domain
700 (TIR) was expressed in bacteria as previously described [85]. Briefly, the TIR domain cloned into
701 the pET-30a(+) vector was transformed into chemically competent *E. coli* BL21(DE3) cells and
702 maintained as a glycerol stock at -80°C. An inoculation loop was used to transfer the transformed
703 bacteria into 5 mL of LB media with 50 µg/mL (final concentration) of kanamycin and the culture
704 was grown overnight at 37°C while rotating. The next day, the cultures were diluted 1:400 in LB
705 media with 50 µg/mL (final concentration) of kanamycin and grown at 37°C while shaking at 215
706 rpm until an $OD_{600}$ of 0.7-0.8 was reached. After cooling, 50 µM IPTG (final concentration) was
707 added to the culture to induce protein expression. The incubator temperature was decreased to
708 16°C and cells were incubated for an additional 16-18 h. Bacterial cells were collected by
709 centrifugation at 3,000 *x g* for 15 min at 4°C, flash frozen in liquid nitrogen, and stored at -80°C
710 until purification.
711 For purification, bacterial pellets were thawed on ice and then resuspended in Lysis Buffer
712 (50 mM Tris•HCl pH 7.0, 300 mM NaCl, 10% (w/v) glycerol, 0.001% Tween 20) with Pierce™
713 EDTA-free protease inhibitor mini tablets (ThermoFisher Scientific). The resuspension was
714 incubated with 100 µg/mL lysozyme for 10 min at 4°C and sonicated with a Fisher Scientific Sonic
715 Dismembrator sonicator (FB-705) in 50-mL batches at an amplitude of 30 for 20 s, pulsing for 1
716 sec on and 1 sec off, followed by a delay period of 20 s for a series of 12 cycles. Crude lysate
717 was clarified at 21,000 *x g* for 25 min at 4°C, at which point the supernatant was applied to pre-
718 equilibrated Strep-Tactin XT Superflow high-capacity resin (IBA Lifesciences) and allowed to
719 enter the column by gravity flow; the Strep-Tactin resin had been equilibrated in Strep Wash
720 Buffer (50 mM Tris•HCl pH 7.0, 300 mM NaCl). The column was washed with 30 column volumes

721 of Strep Wash Buffer and the protein was eluted with 25 column volumes of Strep Elution Buffer
722 (Strep Wash Buffer with 50 mM biotin). Protein eluted from the Strep-Tactin column was then
723 applied to pre-equilibrated TALON Metal Affinity Resin (Takara) and allowed to enter the column
724 by gravity flow; the TALON resin was equilibrated in His Wash 1 (50 mM Tris•HCl pH 7.0, 150
725 mM NaCl, 5 mM imidazole). A series of 15 column volume washes were applied (His Wash 1; His
726 Wash 2: 50 mM Tris•HCl pH 7.0, 150 NaCl, 10 mM imidazole) and the protein was eluted in 20
727 column volumes of His Elution Buffer (50 mM Tris•HCl pH 7.0, 150 mM NaCl, 150 mM imidazole).
728 The eluted protein was dialyzed overnight in Dialysis Buffer (50 mM Tris•HCl, pH 7.0, 150 mM
729 NaCl). The next day, the protein was concentrated using a 10,000 NMWL Amicon Ultra-15
730 Centrifugal Filter Unit at 4°C and the protein concentration was determined by the Bradford assay.
731 TIR was flash frozen in liquid nitrogen and stored at -80°C in 25-μL aliquots.
732
733 **Fluorescent NADase Assay.** Nicotinamide 1,$N^6$-ethenoadenine dinucleotide (ε-NAD, Sigma-
734 Aldrich) is a fluorescent analog of $NAD^+$ and was utilized in kinetic assays as a TIR-1 substrate.
735 TIR-1 cleaves the nicotinamide moiety from ε-NAD to release nicotinamide and etheno-ADPR (ε-
736 ADPR), which fluoresces ($\lambda_{ex}$ = 330 nm, $\lambda_{em}$ = 405 nm). Enzymatic activity was assayed in Assay
737 Buffer (50 mM Tris pH 8.0, 150 mM NaCl; final concentration) using Corning® 96–well Half Area
738 Black Flat Bottom Polystyrene NBS™ Microplates for a final reaction volume of 60-μL, or
739 Corning® 384-well Low Volume Black Round Bottom Polystyrene NBS™ Microplates for a final
740 volume of 20-μL; reactions were initiated by the addition of ε-NAD. ε-ADPR fluorescence intensity
741 readings were taken in real time every 15 sec for 15-30 min using Wallac EnVision Manager
742 Software and a PerkinElmer EnVision 2104 Multilabel Reader. Fluorescence intensity readings
743 ($\lambda_{ex}$ = 330 nm, $\lambda_{em}$ = 405 nm) were converted to [ε-ADPR] with an ε-ADPR standard curve, which
744 was produced by incubating fixed concentrations (0-400 μM) of ε-NAD with excess ADP-ribosyl
745 cyclase and plotting the peak fluorescence intensity values against [ε-ADPR]. The activity was
746 linear with respect to time under all conditions tested.

747

748 **Effect of crowding agents and sodium citrate on the activity of the TIR domain.** The
749 enzymatic activity of the TIR domain was evaluated using the Fluorescent Assay described
750 above. First, the enzyme concentration dependence was determined. For purified protein, the
751 enzyme (0-32.5 μM; final concentration) was added to Assay Buffer in duplicate, briefly incubated
752 at room temperature for 10 min, and the reaction was initiated with 1 mM ε-NAD. Fluorescence
753 intensity was monitored in real time every 15 sec for 15 min.

754 To evaluate the effect of crowding agents and sodium citrate on TIR activity, stock
755 solutions of the additives were made. 50% (w/v) solutions of PEGs 8000, 3500, 1500, and 400,
756 as well as 60% (w/v) solutions of dextran, sucrose, and glycerol were prepared and filtered.
757 Initially, the concentration dependence of TIR in the presence of PEG 3350 was determined. TIR
758 (0-15 μM; final concentration) was added to Assay Buffer with 25% PEG 3350 (final concentration)
759 in duplicate, incubated for 10 min at room temperature, initiated with 1 mM ε-NAD, and monitored
760 every 15 sec for 15 min. The concentration dependence of TIR in 25% PEG 3350 was used to
761 establish that 2.5 μM TIR could be used to enable robust kinetic analyses. Next, the effect of
762 viscogens on TIR activity was evaluated by adding 2.5 μM TIR (final concentration) in duplicate
763 to Assay Buffer with or without 25% w/v of the viscogens (final concentration). Following a brief
764 10 min incubation period, the reaction was initiated with 1 mM ε-NAD and monitored every 15 sec
765 for 20 min. The dose response of 2.5 μM TIR to the viscogens (0, 10, 20, and 30% final
766 concentrations) was evaluated in the same manner and monitored every 15 sec for 15 min.

767 Sodium citrate was prepared as a stock solution of 2 M and filtered. The concentration
768 dependence of TIR in the presence of 500 mM sodium citrate was determined. TIR (0-15 μM;
769 final concentration) was added to Assay Buffer with 500 mM citrate (final concentration) in
770 duplicate, incubated for 10 min at room temperature, and then the reaction was initiated with 1
771 mM ε-NAD and monitored every 15 sec for 15 min. Additionally, the dose dependence of sodium
772 citrate was determined in duplicate. 2.5 μM TIR was added to Assay Buffer with (0-1000 mM)

773 sodium citrate and briefly incubated at room temperature for 10 min. The reaction was initiated
774 with 1 mM E-NAD, and fluorescence was monitored every 15 sec for 15 min.
775 In all cases, the fluorescence intensity was converted to ε-ADPR using the ε-ADPR
776 standard curve described above. Slopes of the progress curves yielded the velocities of the
777 reactions, which were plotted in GraphPad Prism.
778
779 **Effect of PEG 3350 and sodium citrate on steady state kinetics.** Steady state kinetic reactions
780 were carried out in Assay buffer with either PEG 3350 (0-25%; final concentration) or sodium
781 citrate (0-1000 mM; final concentration); a constant concentration of 2.5 μM TIR was used in these
782 assays. Reaction components were mixed in duplicate and incubated at room temperature for 10
783 min before initiating the reaction with ε-NAD (0-4000 μM, final concentration). Fluorescence
784 intensity was monitored every 15 sec for 15 min. Using the ε-ADPR standard curve, the
785 fluorescence was converted to [ε-ADPR]. The velocity of the reactions was calculated from the
786 slope of the progress curve at each ε-NAD concentration and plotted in GraphPad Prism. Kinetic
787 parameters were determined by fitting these velocities to the Michaelis-Menten equation (Eq. 1)
788 at each PEG 3350 or sodium citrate concentration. $K_m$, $k_{cat}$, and $k_{cat}/K_m$ values were plotted against
789 PEG 3350 or sodium citrate concentration.
790 Eq.1 $v = \frac{V_{max}[S]}{K_m+[S]}$,
791 Where $V_{max}$ is the maximum velocity, [$S$] is the substrate concentration, and $K_m$ is the substrate
792 concentration at half the maximum velocity.
793
794 **The TIR domain precipitates in PEG3350 and sodium citrate.** 5 μM TIR was incubated in
795 Assay Buffer with PEG 3350 (0, 10, 17.5, and 25%; final concentration) or sodium citrate (0, 125,
796 250, 500, 750, and 1000 mM; final concentration) in duplicate at room temperature for 15 min.
797 The precentrifugation control was removed and the remainder of the sample was centrifuged at

798 17,000 *x g* at 4 °C for 10 min. Following centrifugation, the supernatant was separated from the
799 pellet and the pellet was resuspended in Assay Buffer with the respective concentration of PEG
800 3350 or sodium citrate. Samples were diluted 1:2 with gel loading buffer and run on an SDS-
801 PAGE gel. Protein bands were stained by Coomassie and visualized on a BioRad Gel Doc EZ
802 Gel Documentation System with Image Lab™ Software. Representative images are shown.
803 Following resuspension of the pellet, all fractions were analyzed in the Fluorescent Assay.
804 After the samples were aliquoted into the assay plate in duplicate, the enzymatic reaction was
805 initiated with 1 mM ε-NAD and monitored every 15 sec for 15 min. Fluorescence intensity was
806 converted to ε-ADPR concentration using the ε-ADPR standard curve. Slopes of the progress
807 curves yielded the velocities of the reactions, which were plotted in GraphPad Prism.
808
809 **Effect of 1,6-hexanediol on TIR domain activity and precipitation.** To evaluate the effect of
810 1,6-hexanediol on TIR activity, the Fluorescent Assay was performed in triplicate in the absence
811 and presence of PEG 3350 or sodium citrate. For pure protein, 35 μM TIR (final concentration)
812 was incubated in Assay Buffer at room temperature for 10 min with or without 2% 1,6-hexanediol
813 (final concentration). For PEG 3350 or citrate, 2.5 μM TIR was incubated in Assay Buffer with
814 25% PEG 3350 or 500 mM sodium citrate (final concentrations) for 10 min at room temperature
815 with or without 2% 1,6-hexanediol. The reactions were initiated with 1 mM ε-NAD and monitored
816 every 15 sec for 15 min. Using the ε-ADPR standard curve, fluorescence was converted to [ε-
817 ADPR] and the reaction velocities (i.e., slopes of the progress curves) obtained. Velocities were
818 normalized for enzyme concentration and these normalized velocities were plotted in GraphPad
819 Prism.
820 To determine whether 1,6-hexanediol can alter TIR precipitation, 1,6-hexanediol was
821 added either before or after TIR precipitation in duplicate. To assess whether 1,6-hexanediol
822 disrupts TIR precipitation, TIR precipitates were formed first by incubating 10 μM TIR (final
823 concentration) with 25% PEG3350 or 500 mM sodium citrate (final concentration) at room

824 temperature for 15 min. 1,6-hexanediol (0, 1, or 2%; final concentrations) was added to the
825 mixture and incubated at room temperature for an additional 10 min. The precentrifugation control
826 was removed and the remaining mixture was centrifuged at 21,000 *x g* for 10 min at 4°C.
827 Supernatant fractions were removed, and the pellet was resuspended in Assay Buffer with the
828 respective additive and concentration of 1,6-hexanediol. All fractions were run on an SDS-PAGE
829 and stained with Coomassie Blue, and gels were imaged on a BioRad Gel Doc EZ Gel
830 Documentation System with Image Lab™ Software. Next, we determined if 1,6-hexanediol could
831 prevent TIR precipitation. 10 μM TIR was incubated in Assay Buffer with 1,6-hexanediol (0, 1, or
832 2%; final concentration) for 15 min at room temperature. 25% PEG 3350 or 500 mM sodium citrate
833 was added to the TIR-buffer-hexanediol mixture and incubated further for 10 min. Controls were
834 removed and the samples were centrifuged at 21,000 *x g* for 10 min at 4°C. As before, supernatant
835 fractions were removed, and pellet fractions were resuspended in Assay Buffer with respective
836 additives and hexanediol concentrations. Fractions were analyzed by SDS-PAGE/Coomassie
837 staining; representative images are shown.
838
839 **Phase Transition Reversibility.** To evaluate the reversibility of the TIR phase transition, 5 μM of
840 TIR was mixed with Assay Buffer and 25% PEG 3350 or 500 mM sodium citrate in duplicate (final
841 concentrations). Following a 15 min incubation period at room temperature, precentrifugation
842 controls were removed and the sample remaining was centrifuged at 17,000 *x g* for 10 min at 4°C.
843 Supernatant fractions were separated from the pellet, which was resuspended in either Assay
844 Buffer alone or Assay Buffer with respective additive. All fractions were analyzed for enzymatic
845 activity in the Fluorescent Assay. Briefly, the precentrifugation, supernatant, and pellet fractions
846 were aliquoted into the assay plates in duplicate and the reaction was initiated with 1 mM ε-NAD.
847 Fluorescence was converted to [ε-ADPR] concentration with the ε-ADPR curve to yield the
848 progress curves. The velocity of the reactions was taken as the slope of the line and the velocities
849 were plotted in GraphPad Prism.

850 To validate the kinetic data, 10 μM TIR (final concentration) was incubated in Assay Buffer
851 with either 25% PEG 3350 or 500 mM sodium citrate (final concentration) for 15 min at room
852 temperature; control samples were incubated in Assay Buffer only. Samples were centrifuged at
853 21,000 *x g* for 10 min at 4°C, after which the supernatant was separated from the pellet. The
854 pellets from samples initially prepared with additives were resuspended in either Assay Buffer
855 alone or Assay Buffer plus the respective additive; this was not necessary for the sample initially
856 prepared without additive since the protein is primarily located in the supernatant in this case.
857 After removing another control sample (Additive lanes on gel), the resuspended samples were
858 centrifuged again at 21,000 *x g* for 10 min at 4°C. As before, the supernatant was removed, and
859 the pellet was resuspended in Assay Buffer with the respective additive. All samples were
860 analyzed for protein content on an SDS-PAGE gel and stained with Coomassie Blue.
861
862 **Effect of pH on TIR domain precipitation and kinetics.** To determine the effect of pH on TIR
863 precipitation, the experiments described above were carried out in duplicate at pH values from
864 4.5-9.0. Briefly, 5 μM TIR (final concentration) was mixed with Assay Buffer (50 mM buffer; 150
865 NaCl) with and without 25% PEG 3350 (final concentration); for pH 4.5-5, sodium acetate buffer
866 was used; for pH 5.5-6.5, MES was used; for pH 7-9, Tris was used. The samples were incubated
867 for 15 min at ambient temperature, at which point the samples were centrifuged at 21,000 *x g* for
868 10 min at 4°C. The supernatant was removed, and the pellet was resuspended in either buffer
869 alone or buffer with 25% PEG 3350 (final concentration); the presence or absence of 25% PEG
870 3350 and the buffer identity of the resuspension solution corresponded to the initial sample
871 preparation. 10-μL 1 M Tris, pH 6.8 was added to each sample to neutralize the buffer before
872 running on an SDS-PAGE gel and staining with Coomassie blue. Images of the gels were
873 obtained on the BioRad Gel Doc EZ Gel Documentation System with Image Lab™ Software.
874 Representative images are shown. ImageJ was used to quantify the bands, which were plotted in
875 GraphPad Prism.

876 Steady state kinetic analyses were also performed at each pH in 25% PEG 3350. A
877 constant concentration of 2.5 μM TIR was used in these assays. Reaction components were
878 mixed in quadruplicate and incubated at room temperature for 10 min before initiating the reaction
879 with 0-2000 μM of ε-NAD (final concentration). Fluorescence intensity was monitored every 15
880 sec for 15 min. Using the ε-ADPR standard curve, the fluorescence was converted to [ε-ADPR].
881 The velocity of the reactions was calculated from the slope of the progress curve at each ε-NAD
882 concentration. Kinetic parameters were determined by fitting these velocities to the Michaelis-
883 Menten equation (Eq. 1) at each pH. The log of $K_m$, $k_{cat}$, and $k_{cat}/K_m$ values were determined and
884 plotted in GraphPad Prism.
885
886 **Negative Stain Electron Microscopy.** Negative stain EM on TIR (270 μg/mL) was performed in
887 Assay Buffer (50 mM Tris, pH 8; 150 mM NaCl) with or without 500 mM sodium citrate. Samples
888 were applied to glow-discharged, carbon- and formvar-coated copper grids and allowed to sit for
889 1 min and 30s before blotting excess liquid away. 1% uranyl acetate was used to fix the samples
890 before image. Samples were images on a FEI Tecnai Spirit 12 microscope. The diameter of
891 particles in the samples with citrate were analyzed in ImageJ.
892
893 **TIR domain mutants.** TIR domain mutants were made using PCR based methods. The pET30a+
894 TIR-1 TIR domain construct was used as a template (0.2-2 ng/μL; final concentration). The
895 manufacturer's protocol for iProof™ High-Fidelity DNA Polymerase (Bio-Rad Laboratories, Inc.)
896 was followed using iProof HF buffer supplemented with 3% DMSO. 50-μL reaction volumes were
897 used in the following protocol: initial denaturation for 3 min at 98°C, denaturation for 45 s at 98°C,
898 annealing for 1:30 min at 45-72 °C, extension for 6 min at 72°C, final extension for 10 min at 72°C.
899 Denaturation, annealing, and extension steps were repeated 30 times. The following day, *Dpn*I
900 was added to the PCR reactions and incubated at 37°C for 2 h to digest the template DNA. The
901 digest was transformed into chemically competent *E. coli* XL1-Blue cells. Transformants were

902 grown overnight in LB media with 50 μg/mL kanamycin and mini-prepped (Promega).
903 Mutagenesis was validated by Sanger sequencing (Genewiz). The mutants were expressed and
904 purified as described for WT TIR.

905 Steady state kinetic analyses of the mutants were carried out in Assay Buffer with 25%
906 PEG 3350 or 500 mM sodium citrate with 2.5 μM of the mutants (final concentrations). Reaction
907 components were mixed in triplicate and incubated at room temperature for 10 min before
908 initiating the reaction with 0-2000 μM of ε-NAD for PEG 3350 or 0-4000 μM for citrate.
909 Fluorescence intensity was monitored every 15 sec for 17.5 min. Using the ε-ADPR standard
910 curve, the fluorescence was converted to [ε-ADPR]. The velocity of the reactions was calculated
911 from the slope of the progress curve at each ε-NAD concentration and plotted in GraphPad Prism.
912 Kinetic parameters were determined by fitting these velocities to the Michaelis-Menten equation
913 (Eq. 1) for each mutant.

914 To evaluate the precipitation capacity of TIR mutants, 10 μM (WT, G747P, E788Q, and
915 H833A) or 3 μM (WT, E788A) of the enzyme was mixed with Assay Buffer (50 mM Tris, pH 8.0;
916 150 NaCl) with and without 25% PEG 3350 or 500 mM sodium citrate (final concentrations).
917 Precipitation of the $TIR^{E788A}$ mutant was evaluated at 3 μM due to low yields of the protein; WT
918 TIR at 3 μM was included as the proper control. The samples were incubated for 15 min at ambient
919 temperature, at which point the samples were centrifuged at 21,000 *x g* for 10 min at 4°C. The
920 supernatant was removed, and the pellet was resuspended buffer with the respective additive
921 (final concentration). Samples were diluted 1:1 with water before running on an SDS-PAGE gel.
922 Stain free images of the gels were obtained on the BioRad Gel Doc EZ Gel Documentation
923 System with Image Lab™ Software. Representative images are shown. ImageJ was used to
924 quantify the bands, which were plotted in GraphPad Prism.
925

926 **Statistical Analyses.** Differences in survival of *C. elegans* in the *P. aeruginosa* pathogenesis
927 assays were determined with the log-rank test after survival curves were estimated for each group
928 with the Kaplan-Meier method. OASIS 2 was used for these statistical analyses [86]. qRT-PCR
929 studies, intestinal CFU quantification, western blot band intensity quantification, TIR NADase
930 activity, and TIR protein precipitation are presented as the mean ± standard error of the mean.
931 Statistical hypothesis testing was performed with Prism 9 (GraphPad Software) using methods
932 indicated in the figure legends. Sample sizes, mean lifespan, and p-values for all trials are shown
933 in Table S2.

934

935 **Data Availability.** The mRNA-seq dataset is available from the NCBI Gene Expression Omnibus
936 using the accession number GSE178572. All other data are available in the manuscript.

937

938 **REFERENCES**


939 1. Kim DH, Feinbaum R, Alloing G, Emerson FE, Garsin DA, Inoue H, et al. A conserved p38
940 MAP kinase pathway in *Caenorhabditis elegans* innate immunity. Science. 2002;297(5581):623-
941 6. doi: 10.1126/science.1073759. PubMed PMID: 12142542.
942
943 2. Liberati NT, Fitzgerald KA, Kim DH, Feinbaum R, Golenbock DT, Ausubel FM. Requirement
944 for a conserved Toll/interleukin-1 resistance domain protein in the *Caenorhabditis elegans*
945 immune response. Proc Natl Acad Sci USA. 2004;101(17):6593-8. doi:
946 10.1073/pnas.0308625101. PubMed PMID: 15123841.
947
948 3. Couillault C, Pujol N, Reboul J, Sabatier L, Guichou JF, Kohara Y, et al. TLR-independent
949 control of innate immunity in *Caenorhabditis elegans* by the TIR domain adaptor protein TIR-1,
950 an ortholog of human SARM. Nat Immunol. 2004;5(5):488-94. doi: 10.1038/ni1060. PubMed
951 PMID: 15048112.
952
953 4. Troemel ER, Chu SW, Reinke V, Lee SS, Ausubel FM, Kim DH. p38 MAPK regulates
954 expression of immune response genes and contributes to longevity in *C. elegans*. PLoS Genet.
955 2006;2(11):e183. Epub 2006/11/14. doi: 06-PLGE-RA-0292R2 [pii]
956 10.1371/journal.pgen.0020183. PubMed PMID: 17096597.
957
958 5. Peterson ND, Pukkila-Worley R. *Caenorhabditis elegans* in high-throughput screens for anti-
959 infective compounds. Curr Opin Immunol. 2018;54:59-65. Epub 2018/06/24. doi:
960 10.1016/j.coi.2018.06.003. PubMed PMID: 29935375.
961
962 6. Pukkila-Worley R, Ausubel FM. Immune defense mechanisms in the *Caenorhabditis elegans*
963 intestinal epithelium. Curr Opin Immunol. 2012;24(1):3-9. doi: 10.1016/j.coi.2011.10.004.
964 PubMed PMID: 22236697.
965
966 7. Du M, Chen ZJ. DNA-induced liquid phase condensation of cGAS activates innate immune
967 signaling. Science. 2018;361(6403):704-9. Epub 2018/07/07. doi: 10.1126/science.aat1022.
968 PubMed PMID: 29976794.
969
970 8. Chen D, Wang Z, Zhao YG, Zheng H, Zhao H, Liu N, et al. Inositol Polyphosphate
971 Multikinase Inhibits Liquid-Liquid Phase Separation of TFEB to Negatively Regulate Autophagy
972 Activity. Dev Cell. 2020;55(5):588-602 e7. Epub 2020/12/09. doi: 10.1016/j.devcel.2020.10.010.
973 PubMed PMID: 33290695.
974
975 9. Alberti S, Gladfelter A, Mittag T. Considerations and Challenges in Studying Liquid-Liquid
976 Phase Separation and Biomolecular Condensates. Cell. 2019;176(3):419-34. Epub 2019/01/27.
977 doi: 10.1016/j.cell.2018.12.035. PubMed PMID: 30682370.
978
979 10. Boeynaems S, Alberti S, Fawzi NL, Mittag T, Polymenidou M, Rousseau F, et al. Protein
980 Phase Separation: A New Phase in Cell Biology. Trends Cell Biol. 2018;28(6):420-35. Epub
981 2018/04/01. doi: 10.1016/j.tcb.2018.02.004. PubMed PMID: 29602697.
982
983 11. Alberti S, Dormann D. Liquid-Liquid Phase Separation in Disease. Annu Rev Genet.
984 2019;53:171-94. Epub 2019/08/21. doi: 10.1146/annurev-genet-112618-043527. PubMed
985 PMID: 31430179.
986

12. Patel A, Lee HO, Jawerth L, Maharana S, Jahnel M, Hein MY, et al. A Liquid-to-Solid Phase Transition of the ALS Protein FUS Accelerated by Disease Mutation. Cell. 2015;162(5):1066-77. Epub 2015/09/01. doi: 10.1016/j.cell.2015.07.047. PubMed PMID: 26317470.

13. Verdile V, De Paola E, Paronetto MP. Aberrant Phase Transitions: Side Effects and Novel Therapeutic Strategies in Human Disease. Front Genet. 2019;10:173. Epub 2019/04/11. doi: 10.3389/fgene.2019.00173. PubMed PMID: 30967892.

14. Kroschwald S, Maharana S, Mateju D, Malinovska L, Nuske E, Poser I, et al. Promiscuous interactions and protein disaggregases determine the material state of stress-inducible RNP granules. Elife. 2015;4:e06807. Epub 2015/08/05. doi: 10.7554/eLife.06807. PubMed PMID: 26238190.

15. Loring HS, Czech VL, Icso JD, O'Connor L, Parelkar SS, Byrne AB, et al. A phase transition enhances the catalytic activity of SARM1, an NAD(+) glycohydrolase involved in neurodegeneration. Elife. 2021;10. Epub 2021/06/30. doi: 10.7554/eLife.66694. PubMed PMID: 34184985.

16. Marion CM, McDaniel DP, Armstrong RC. Sarm1 deletion reduces axon damage, demyelination, and white matter atrophy after experimental traumatic brain injury. Exp Neurol. 2019;321:113040. Epub 2019/08/25. doi: 10.1016/j.expneurol.2019.113040. PubMed PMID: 31445042.

17. Henninger N, Bouley J, Sikoglu EM, An J, Moore CM, King JA, et al. Attenuated traumatic axonal injury and improved functional outcome after traumatic brain injury in mice lacking Sarm1. Brain. 2016;139(Pt 4):1094-105. Epub 2016/02/26. doi: 10.1093/brain/aww001. PubMed PMID: 26912636.

18. Geisler S, Doan RA, Strickland A, Huang X, Milbrandt J, DiAntonio A. Prevention of vincristine-induced peripheral neuropathy by genetic deletion of SARM1 in mice. Brain. 2016;139(Pt 12):3092-108. Epub 2016/11/01. doi: 10.1093/brain/aww251. PubMed PMID: 27797810.

19. Hieb WF, Rothstein M. Sterol requirement for reproduction of a free-living nematode. Science. 1968;160(3829):778-80. Epub 1968/05/17. doi: 10.1126/science.160.3829.778. PubMed PMID: 4869093.

20. Chitwood DJ. Biochemistry and function of nematode steroids. Crit Rev Biochem Mol Biol. 1999;34(4):273-84. Epub 1999/10/12. doi: 10.1080/10409239991209309. PubMed PMID: 10517647.

21. Shim YH, Chun JH, Lee EY, Paik YK. Role of cholesterol in germ-line development of *Caenorhabditis elegans*. Mol Reprod Dev. 2002;61(3):358-66. Epub 2002/02/09. doi: 10.1002/mrd.10099. PubMed PMID: 11835581.

22. Merris M, Wadsworth WG, Khamrai U, Bittman R, Chitwood DJ, Lenard J. Sterol effects and sites of sterol accumulation in *Caenorhabditis elegans*: developmental requirement for 4alpha-methyl sterols. J Lipid Res. 2003;44(1):172-81. Epub 2003/01/09. doi: 10.1194/jlr.m200323-jlr200. PubMed PMID: 12518036.

23. Yochem J, Tuck S, Greenwald I, Han M. A gp330/megalin-related protein is required in the major epidermis of *Caenorhabditis elegans* for completion of molting. Development. 1999;126(3):597-606. Epub 1999/01/07. PubMed PMID: 9876188.

24. Otarigho B, Aballay A. Cholesterol Regulates Innate Immunity via Nuclear Hormone Receptor NHR-8. iScience. 2020;23(5):101068. Epub 2020/05/04. doi: 10.1016/j.isci.2020.101068. PubMed PMID: 32361270.

25. Cheong MC, Na K, Kim H, Jeong SK, Joo HJ, Chitwood DJ, et al. A potential biochemical mechanism underlying the influence of sterol deprivation stress on *Caenorhabditis elegans* longevity. J Biol Chem. 2011;286(9):7248-56. Epub 2010/12/28. doi: 10.1074/jbc.M110.189183. PubMed PMID: 21186286.

26. Burnell AM, Houthoofd K, O'Hanlon K, Vanfleteren JR. Alternate metabolism during the dauer stage of the nematode *Caenorhabditis elegans*. Exp Gerontol. 2005;40(11):850-6. Epub 2005/10/14. doi: 10.1016/j.exger.2005.09.006. PubMed PMID: 16221538.

27. Vanfleteren JR, De Vreese A. Rate of aerobic metabolism and superoxide production rate potential in the nematode *Caenorhabditis elegans*. J Exp Zool. 1996;274(2):93-100. Epub 1996/02/01. doi: 10.1002/(SICI)1097-010X(19960201)274:2<93::AID-JEZ2>3.0.CO;2-8. PubMed PMID: 8742689.

28. Gerisch B, Weitzel C, Kober-Eisermann C, Rottiers V, Antebi A. A hormonal signaling pathway influencing *C. elegans* metabolism, reproductive development, and life span. Dev Cell. 2001;1(6):841-51. Epub 2001/12/13. doi: 10.1016/s1534-5807(01)00085-5. PubMed PMID: 11740945.

29. Gerisch B, Antebi A. Hormonal signals produced by DAF-9/cytochrome P450 regulate *C. elegans* dauer diapause in response to environmental cues. Development. 2004;131(8):1765-76. Epub 2004/04/16. doi: 10.1242/dev.01068. PubMed PMID: 15084461.

30. Motola DL, Cummins CL, Rottiers V, Sharma KK, Li T, Li Y, et al. Identification of ligands for DAF-12 that govern dauer formation and reproduction in *C. elegans*. Cell. 2006;124(6):1209-23. Epub 2006/03/15. doi: 10.1016/j.cell.2006.01.037. PubMed PMID: 16529801.

31. Brenner S. The genetics of *Caenorhabditis elegans*. Genetics. 1974;77(1):71-94. Epub 1974/05/01. PubMed PMID: 4366476.

32. Shivers RP, Kooistra T, Chu SW, Pagano DJ, Kim DH. Tissue-specific activities of an immune signaling module regulate physiological responses to pathogenic and nutritional bacteria in *C. elegans*. Cell Host Microbe. 2009;6(4):321-30. Epub 2009/10/20. doi: S1931-3128(09)00310-2 [pii]10.1016/j.chom.2009.09.001. PubMed PMID: 19837372.

33. Bolz DD, Tenor JL, Aballay A. A conserved PMK-1/p38 MAPK is required in *Caenorhabditis elegans* tissue-specific immune response to *Yersinia pestis* infection. J Biol Chem. 2010;285(14):10832-40. doi: 10.1074/jbc.M109.091629. PubMed PMID: 20133945.

34. Magner DB, Wollam J, Shen Y, Hoppe C, Li D, Latza C, et al. The NHR-8 nuclear receptor regulates cholesterol and bile acid homeostasis in *C. elegans*. Cell Metab. 2013;18(2):212-24. Epub 2013/08/13. doi: 10.1016/j.cmet.2013.07.007. PubMed PMID: 23931753.

35. Lindblom TH, Pierce GJ, Sluder AE. A *C. elegans* orphan nuclear receptor contributes to xenobiotic resistance. Curr Biol. 2001;11(11):864-8. Epub 2001/08/23. doi: 10.1016/s0960-9822(01)00236-6. PubMed PMID: 11516648.

36. Shivers RP, Pagano DJ, Kooistra T, Richardson CE, Reddy KC, Whitney JK, et al. Phosphorylation of the conserved transcription factor ATF-7 by PMK-1 p38 MAPK regulates innate immunity in *Caenorhabditis elegans*. PLoS Genet. 2010;6(4):e1000892. Epub 2010/04/07. doi: 10.1371/journal.pgen.1000892. PubMed PMID: 20369020.

37. Inoue H, Hisamoto N, An JH, Oliveira RP, Nishida E, Blackwell TK, et al. The *C. elegans* p38 MAPK pathway regulates nuclear localization of the transcription factor SKN-1 in oxidative stress response. Genes Dev. 2005;19(19):2278-83. Epub 2005/09/17. doi:10.1101/gad.1324805. PubMed PMID: 16166371.

38. Kim DH, Liberati NT, Mizuno T, Inoue H, Hisamoto N, Matsumoto K, et al. Integration of *Caenorhabditis elegans* MAPK pathways mediating immunity and stress resistance by MEK-1 MAPK kinase and VHP-1 MAPK phosphatase. Proc Natl Acad Sci USA. 2004;101(30):10990-4. doi: 10.1073/pnas.0403546101. PubMed PMID: 15256594.

39. Powell JR, Kim DH, Ausubel FM. The G protein-coupled receptor FSHR-1 is required for the *Caenorhabditis elegans* innate immune response. Proc Natl Acad Sci U S A. 2009;106(8):2782-7. Epub 2009/02/07. doi: 0813048106 [pii]10.1073/pnas.0813048106. PubMed PMID: 19196974.

40. Garsin DA, Villanueva JM, Begun J, Kim DH, Sifri CD, Calderwood SB, et al. Long-lived *C. elegans daf-2* mutants are resistant to bacterial pathogens. Science. 2003;300(5627):1921. doi: 10.1126/science.1080147. PubMed PMID: 12817143.

41. Chuang CF, Bargmann CI. A Toll-interleukin 1 repeat protein at the synapse specifies asymmetric odorant receptor expression via ASK1 MAPKKK signaling. Genes Dev. 2005;19(2):270-81. Epub 2004/12/31. doi: 10.1101/gad.1276505. PubMed PMID: 15625192.

42. Horsefield S, Burdett H, Zhang X, Manik MK, Shi Y, Chen J, et al. NAD(+) cleavage activity by animal and plant TIR domains in cell death pathways. Science. 2019;365(6455):793-9. Epub 2019/08/24. doi: 10.1126/science.aax1911. PubMed PMID: 31439792.

43. Wan L, Essuman K, Anderson RG, Sasaki Y, Monteiro F, Chung EH, et al. TIR domains of plant immune receptors are NAD(+)-cleaving enzymes that promote cell death. Science. 2019;365(6455):799-803. Epub 2019/08/24. doi: 10.1126/science.aax1771. PubMed PMID: 31439793.

44. Summers DW, Gibson DA, DiAntonio A, Milbrandt J. SARM1-specific motifs in the TIR domain enable NAD+ loss and regulate injury-induced SARM1 activation. Proc Natl Acad Sci U S A. 2016;113(41):E6271-e80. Epub 2016/09/28. doi: 10.1073/pnas.1601506113. PubMed PMID: 27671644.

45. Essuman K, Summers DW, Sasaki Y, Mao X, DiAntonio A, Milbrandt J. The SARM1 Toll/Interleukin-1 Receptor Domain Possesses Intrinsic NAD(+) Cleavage Activity that Promotes Pathological Axonal Degeneration. Neuron. 2017;93(6):1334-43.e5. Epub 2017/03/24. doi: 10.1016/j.neuron.2017.02.022. PubMed PMID: 28334607.

46. Gadda G, Sobrado P. Kinetic Solvent Viscosity Effects as Probes for Studying the Mechanisms of Enzyme Action. Biochemistry. 2018;57(25):3445-53. Epub 2018/06/07. doi: 10.1021/acs.biochem.8b00232. PubMed PMID: 29874467.

47. Blacklow SC, Raines RT, Lim WA, Zamore PD, Knowles JR. Triosephosphate isomerase catalysis is diffusion controlled. Appendix: Analysis of triose phosphate equilibria in aqueous solution by 31P NMR. Biochemistry. 1988;27(4):1158-67. Epub 1988/02/23. doi: 10.1021/bi00404a013. PubMed PMID: 3365378.

48. Rivas G, Minton AP. Macromolecular Crowding In Vitro, In Vivo, and In Between. Trends Biochem Sci. 2016;41(11):970-81. Epub 2016/10/30. doi: 10.1016/j.tibs.2016.08.013. PubMed PMID: 27669651.

49. Peskett TR, Rau F, O'Driscoll J, Patani R, Lowe AR, Saibil HR. A Liquid to Solid Phase Transition Underlying Pathological Huntingtin Exon1 Aggregation. Mol Cell. 2018;70(4):588-601 e6. Epub 2018/05/15. doi: 10.1016/j.molcel.2018.04.007. PubMed PMID: 29754822.

50. Peterson ND, Cheesman HK, Liu P, Anderson SM, Foster KJ, Chhaya R, et al. The nuclear hormone receptor NHR-86 controls anti-pathogen responses in *C. elegans*. PLoS Genet. 2019;15(1):e1007935. Epub 2019/01/23. doi: 10.1371/journal.pgen.1007935. PubMed PMID: 30668573.

51. Sluder AE, Mathews SW, Hough D, Yin VP, Maina CV. The nuclear receptor superfamily has undergone extensive proliferation and diversification in nematodes. Genome Res. 1999;9(2):103-20. PubMed PMID: 10022975.

52. Sluder AE, Maina CV. Nuclear receptors in nematodes: themes and variations. Trends Genet. 2001;17(4):206-13. PubMed PMID: 11275326.

53. Pujol N, Cypowyj S, Ziegler K, Millet A, Astrain A, Goncharov A, et al. Distinct innate immune responses to infection and wounding in the *C. elegans* epidermis. Curr Biol. 2008;18(7):481-9. doi: 10.1016/j.cub.2008.02.079. PubMed PMID: 18394898.

54. Tecle E, Chhan CB, Franklin L, Underwood RS, Hanna-Rose W, Troemel ER. The purine nucleoside phosphorylase *pnp-1* regulates epithelial cell resistance to infection in *C. elegans*. PLoS Pathog. 2021;17(4):e1009350. Epub 2021/04/21. doi: 10.1371/journal.ppat.1009350. PubMed PMID: 33878133.

55. Foster KJ, Cheesman HK, Liu P, Peterson ND, Anderson SM, Pukkila-Worley R. Innate Immunity in the *C. elegans* Intestine Is Programmed by a Neuronal Regulator of AWC Olfactory Neuron Development. Cell Rep. 2020;31(1):107478. Epub 2020/04/09. doi: 10.1016/j.celrep.2020.03.042. PubMed PMID: 32268082.

56. Wu Z, Isik M, Moroz N, Steinbaugh MJ, Zhang P, Blackwell TK. Dietary Restriction Extends Lifespan through Metabolic Regulation of Innate Immunity. Cell Metab. 2019;29(5):1192-205 e8. Epub 2019/03/25. doi: 10.1016/j.cmet.2019.02.013. PubMed PMID: 30905669.

57. Anderson SM, Pukkila-Worley R. Immunometabolism in *Caenorhabditis elegans*. PLoS Pathog. 2020;16(10):e1008897. Epub 2020/10/09. doi: 10.1371/journal.ppat.1008897. PubMed PMID: 33031414.

58. Gerdts J, Brace EJ, Sasaki Y, DiAntonio A, Milbrandt J. SARM1 activation triggers axon degeneration locally via NAD(+) destruction. Science. 2015;348(6233):453-7. Epub 2015/04/25. doi: 10.1126/science.1258366. PubMed PMID: 25908823.

59. Gerdts J, Summers DW, Sasaki Y, DiAntonio A, Milbrandt J. Sarm1-mediated axon degeneration requires both SAM and TIR interactions. J Neurosci. 2013;33(33):13569-80. Epub 2013/08/16. doi: 10.1523/jneurosci.1197-13.2013. PubMed PMID: 23946415.

60. Mizuno T, Hisamoto N, Terada T, Kondo T, Adachi M, Nishida E, et al. The *Caenorhabditis elegans* MAPK phosphatase VHP-1 mediates a novel JNK-like signaling pathway in stress response. EMBO J. 2004;23(11):2226-34. doi: 10.1038/sj.emboj.7600226. PubMed PMID: 15116070.

61. Pukkila-Worley R, Feinbaum RL, McEwan DL, Conery AL, Ausubel FM. The evolutionarily conserved mediator subunit MDT-15/MED15 links protective innate immune responses and xenobiotic detoxification. PLoS Pathog. 2014;10(5):e1004143. doi: 10.1371/journal.ppat.1004143. PubMed PMID: 24875643.

62. Rahme LG, Stevens EJ, Wolfort SF, Shao J, Tompkins RG, Ausubel FM. Common virulence factors for bacterial pathogenicity in plants and animals. Science. 1995;268(5219):1899-902. Epub 1995/06/30. PubMed PMID: 7604262.

63. Anderson SM, Cheesman HK, Peterson ND, Salisbury JE, Soukas AA, Pukkila-Worley R. The fatty acid oleate is required for innate immune activation and pathogen defense in Caenorhabditis elegans. PLoS Pathog. 2019;15(6):e1007893. Epub 2019/06/18. doi: 10.1371/journal.ppat.1007893. PubMed PMID: 31206555.

64. Nandakumar M, Tan MW. Gamma-Linolenic and Stearidonic Acids Are Required for Basal Immunity in *Caenorhabditis elegans* through Their Effects on p38 MAP Kinase Activity. PLoS Genet. 2008;4(11):e1000273. doi: 10.1371/journal.pgen.1000273. PubMed PMID: 19023415.

65. Dokshin GA, Ghanta KS, Piscopo KM, Mello CC. Robust Genome Editing with Short Single-Stranded and Long, Partially Single-Stranded DNA Donors in *Caenorhabditis elegans*. Genetics. 2018;210(3):781-7. Epub 2018/09/15. doi: 10.1534/genetics.118.301532. PubMed PMID: 30213854.

66. Ghanta KS, Mello CC. Melting dsDNA Donor Molecules Greatly Improves Precision Genome Editing in *Caenorhabditis elegans*. Genetics. 2020;216(3):643-50. Epub 2020/09/24. doi: 10.1534/genetics.120.303564. PubMed PMID: 32963112.

67. Labun K, Montague TG, Krause M, Torres Cleuren YN, Tjeldnes H, Valen E. CHOPCHOP v3: expanding the CRISPR web toolbox beyond genome editing. Nucleic Acids Res. 2019;47(W1):W171-W4. Epub 2019/05/21. doi: 10.1093/nar/gkz365. PubMed PMID: 31106371.

68. Fire A, Xu S, Montgomery MK, Kostas SA, Driver SE, Mello CC. Potent and specific genetic interference by double-stranded RNA in *Caenorhabditis elegans*. Nature. 1998;391(6669):806-11. Epub 1998/03/05. doi: 10.1038/35888. PubMed PMID: 9486653.

69. Timmons L, Court DL, Fire A. Ingestion of bacterially expressed dsRNAs can produce specific and potent genetic interference in *Caenorhabditis elegans*. Gene. 2001;263(1-2):103-12. Epub 2001/02/27. doi: 10.1016/s0378-1119(00)00579-5. PubMed PMID: 11223248.

70. Conte D, Jr., MacNeil LT, Walhout AJM, Mello CC. RNA Interference in *Caenorhabditis elegans*. Curr Protoc Mol Biol. 2015;109:26 3 1- 3 30. Epub 2015/01/07. doi: 10.1002/0471142727.mb2603s109. PubMed PMID: 25559107.

71. Tan MW, Mahajan-Miklos S, Ausubel FM. Killing of *Caenorhabditis elegans* by *Pseudomonas aeruginosa* used to model mammalian bacterial pathogenesis. Proc Natl Acad Sci USA. 1999;96(2):715-20. PubMed PMID: 9892699.

72. Foster KJ, McEwan DL, Pukkila-Worley R. Measurements of Innate Immune Function in *C. elegans*. Methods Mol Biol. 2020;2144:145-60. Epub 2020/05/16. doi: 10.1007/978-1-0716-0592-9_13. PubMed PMID: 32410032.

73. Singh J, Aballay A. Microbial Colonization Activates an Immune Fight-and-Flight Response via Neuroendocrine Signaling. Dev Cell. 2019;49(1):89-99 e4. Epub 2019/03/05. doi: 10.1016/j.devcel.2019.02.001. PubMed PMID: 30827896.

74. Bray NL, Pimentel H, Melsted P, Pachter L. Near-optimal probabilistic RNA-seq quantification. Nat Biotechnol. 2016;34(5):525-7. Epub 2016/04/05. doi: 10.1038/nbt.3519. PubMed PMID: 27043002.

75. Pimentel H, Bray NL, Puente S, Melsted P, Pachter L. Differential analysis of RNA-seq incorporating quantification uncertainty. Nat Methods. 2017;14(7):687-90. Epub 2017/06/06. doi: 10.1038/nmeth.4324. PubMed PMID: 28581496.

76. Cheng X, Yan J, Liu Y, Wang J, Taubert S. eVITTA: a web-based visualization and inference toolbox for transcriptome analysis. Nucleic Acids Res. 2021;49(W1):W207-W15. Epub 2021/05/22. doi: 10.1093/nar/gkab366. PubMed PMID: 34019643.

77. Huang da W, Sherman BT, Lempicki RA. Systematic and integrative analysis of large gene lists using DAVID bioinformatics resources. Nat Protoc. 2009;4(1):44-57. Epub 2009/01/10. doi: nprot.2008.211 [pii]10.1038/nprot.2008.211. PubMed PMID: 19131956.

78. Subramanian A, Tamayo P, Mootha VK, Mukherjee S, Ebert BL, Gillette MA, et al. Gene set enrichment analysis: a knowledge-based approach for interpreting genome-wide expression profiles. Proc Natl Acad Sci U S A. 2005;102(43):15545-50. Epub 2005/10/04. doi: 10.1073/pnas.0506580102. PubMed PMID: 16199517.

79. Fletcher M, Tillman EJ, Butty VL, Levine SS, Kim DH. Global transcriptional regulation of innate immunity by ATF-7 in *C. elegans*. PLoS Genet. 2019;15(2):e1007830. Epub 2019/02/23. doi: 10.1371/journal.pgen.1007830. PubMed PMID: 30789901.

80. Taubert S, Hansen M, Van Gilst MR, Cooper SB, Yamamoto KR. The Mediator subunit MDT-15 confers metabolic adaptation to ingested material. PLoS Genet. 2008;4(2):e1000021. doi: 10.1371/journal.pgen.1000021. PubMed PMID: 18454197.

81. Richardson CE, Kooistra T, Kim DH. An essential role for XBP-1 in host protection against immune activation in *C. elegans*. Nature. 2010;463(7284):1092-5. Epub 2010/02/26. doi: nature08762 [pii]10.1038/nature08762. PubMed PMID: 20182512.

82. Estes KA, Dunbar TL, Powell JR, Ausubel FM, Troemel ER. bZIP transcription factor *zip-2* mediates an early response to *Pseudomonas aeruginosa* infection in *Caenorhabditis elegans*. Proc Natl Acad Sci U S A. 2010;107(5):2153-8. Epub 2010/02/06. doi: 0914643107 [pii] 10.1073/pnas.0914643107. PubMed PMID: 20133860.

83. Pfaffl MW. A new mathematical model for relative quantification in real-time RT-PCR. Nucleic Acids Res. 2001;29(9):e45. Epub 2001/05/09. PubMed PMID: 11328886.

84. Cheesman HK, Feinbaum RL, Thekkiniath J, Dowen RH, Conery AL, Pukkila-Worley R. Aberrant Activation of p38 MAP Kinase-Dependent Innate Immune Responses Is Toxic to *Caenorhabditis elegans*. G3 (Bethesda). 2016;6(3):541-9. doi: 10.1534/g3.115.025650. PubMed PMID: 26818074.

85. Loring HS, Icso JD, Nemmara VV, Thompson PR. Initial Kinetic Characterization of Sterile Alpha and Toll/Interleukin Receptor Motif-Containing Protein 1. Biochemistry. 2020;59(8):933-42. Epub 2020/02/13. doi: 10.1021/acs.biochem.9b01078. PubMed PMID: 32049506.

86. Han SK, Lee D, Lee H, Kim D, Son HG, Yang JS, et al. OASIS 2: online application for survival analysis 2 with features for the analysis of maximal lifespan and healthspan in aging research. Oncotarget. 2016;7(35):56147-52. Epub 2016/08/17. doi: 10.18632/oncotarget.11269. PubMed PMID: 27528229.

1313 **Figure 1. Cholesterol scarcity activates intestinal innate immune defenses.** Images of
1314 T24B8.5p::*gfp* **(A)** and *irg-5*p::*GFP* **(B)** transcriptional immune reporters in wild-type animals
1315 growing on standard nematode growth media (+5 µg/mL cholesterol) and in the absence of
1316 supplemented cholesterol (+0 µg/mL cholesterol). **(C)** qRT-PCR data of the indicated innate
1317 immune effector genes in wild-type *C. elegans* growing in the presence (+5 µg/mL) and absence
1318 (+0 µg/mL) of supplemented cholesterol. *equals $p<0.05$ (unpaired t-test). **(D and E)** Data from
1319 mRNA-seq experiments comparing genes differentially regulated in uninfected *nhr-8(hd117)*
1320 mutants versus wild-type animals **(D)** or uninfected wild-type animals grown in the absence (0
1321 µg/mL) versus presence (5 µg/mL) of supplemental cholesterol **(E)** (y-axis) are compared with
1322 genes differentially expressed in wild-type animals during *P. aeruginosa* infection (x-axis). All
1323 genes are shown in gray. Genes that are differentially expressed in both datasets are shown in
1324 black (Fold change >2, $q<0.01$). Genes that are annotated as innate immune genes are shown in
1325 red. The location of the representative genes T24B8.5, *irg*-5, irg-*4*, and K08D8.4, whose
1326 expression is examined throughout this manuscript are shown. See also Tables S1A-C. **(F, G, H)**
1327 Images of T24B8.5p::*gfp* animals of the indicted genotypes, grown under the indicated conditions
1328 are shown. **(H)** *C. elegans* were grown on media solidified with agarose, rather than agar. **(I, J,**
1329 **K, L)** qRT-PCR data of the indicated genes in wild-type and *nhr-8(hd117)* mutant animals grown
1330 on standard nematode growth media (+5 µg/mL cholesterol) in the presence or absence of 0.1%
1331 Tergitol, as indicated. For the qRT-PCR studies in Figs. 1C, 1I, 1J, 1K, and 1L**,** data are the
1332 average of three independent biological replicates, each normalized to a control gene with error
1333 bars representing SEM and are presented as the value relative to the average expression from
1334 all replicates of the indicated gene in wild-type animals on standard nematode growth media (+5
1335 µg/mL cholesterol). *equals $p<0.05$ (two-way ANOVA with Tukey multiple comparison testing).
1336 **(M, N)** *C. elegans* pathogenesis assay with *P. aeruginosa* and *C. elegans* of indicated genotypes
1337 at the L4 larval stage is shown and exposed to the indicated conditions. Data are representative
1338 of three trials. The Kaplan-Meier method was used to estimate the survival curves for each group,
1339 and the log rank test was used for all statistical comparisons. Sample sizes, mean lifespan and
1340 p-values for all trials are shown in Table S2. **(O)** *P. aeruginosa,* isolated from the intestines of
1341 animals with the indicated genotypes, were quantified after 24 hours of bacterial infection. Data
1342 are colony forming units (CFU) of *P. aeruginosa* and are presented as the average of 10 separate
1343 biological replicates with each replicate containing 10-11 animals. *equals $p<0.05$ (unpaired t-
1344 test). Scale bars in all images equal 200 µm. See also Fig. S1.

1345 **Figure 2. Cholesterol scarcity activates the p38 PMK-1 innate immune pathway. (A)** Gene
1346 set enrichment analysis (GSEA) of p38 PMK-1 targets in the 0 µg/mL cholesterol mRNA-seq
1347 experiment. Fold change in expression of significantly differentially expressed genes (fold-change
1348 >2 and q<0.01) in uninfected animals grown in the absence (0 µg/mL) versus presence (5 µg/mL)
1349 of supplemental cholesterol are ranked from higher expression (red) to lower expression (blue).
1350 Normalized enrichment score (NES) and q-value are indicated. p38 PMK-1 targets found in the
1351 transcriptional profile are indicated by hit number (116) in the left margin and black lines. **(B)** An
1352 immunoblot analysis of lysates from wild-type *C. elegans* grown on standard nematode growth
1353 media in the presence (+5 µg/mL cholesterol) and in the absence (+0 µg/mL cholesterol) of
1354 supplemented cholesterol using antibodies that recognize the doubly phosphorylated TGY motif
1355 of PMK-1 (phos-PMK-1), total PMK-1 protein (total PMK-1) and tubulin (α-tubulin) is shown. PMK-
1356 1 is a 43.9 kDa protein and tubulin is a 50 kDa protein. **(C)** The band intensities of four biological
1357 replicates of the Western blot shown in Fig. 2A were quantified. *equals p<0.05 (unpaired t-test)
1358 **(D)** GSEA of p38 PMK-1 targets in the *nhr-8* mRNA-seq experiment as described in Fig. 2A. **(E,**
1359 **F)** Western blot experiment and quantification of four biological replicate experiments as
1360 described in Fig. 2B and Fig. 2C with the strains of the indicated genotypes. In Fig. 2B and Fig.
1361 2E**,** *pmk-1(km25)* and *nsy-1(ag3)* and loss-of-function mutants are the controls, which confirm
1362 specificity of phos-PMK-1 and total PMK-1 probing. *equals p<0.05 (one-way ANOVA with
1363 Dunnett multiple comparison testing). **(G)** Images of T24B8.5p::*gfp* transcriptional immune
1364 reporter animals in wild-type animals and *nhr-8(hd117)* mutants growing on control RNAi, *tir-*
1365 *1(RNAi)* or *atf-7(RNAi)* bacteria, as indicated. **(H, I, J, K)** qRT-PCR data of the indicated genes in
1366 the indicated mutant animals grown on standard nematode growth media (+5 µg/mL cholesterol).
1367 Data are the average of three to seven independent replicates, each normalized to a control gene
1368 with error bars representing SEM and are presented as the value relative to the average
1369 expression from all replicates of the indicated gene in wild-type animals. *equals p<0.05 (one-
1370 way ANOVA with Dunnett multiple comparison testing) **(L)** Images of T24B8.5p::*gfp*
1371 transcriptional immune reporter animals of the indicated genotypes growing in the presence or
1372 absence of 0.1% Tergitol. Scale bars in all images equal 200 µm. See also Fig. S2.

1373 **Figure 3. Activation of the p38 PMK-1 pathway by cholesterol deprivation requires TIR-1**
1374 **oligomerization and NADase activity. (A)** Model of *tir-1* showing the domains and the mutations
1375 that were introduced using CRISPR-Cas9. **(B, C, D)** Expression of the innate immune effector
1376 T24B8.5p::*gfp* in *tir-1* mutants with predicted defects in oligomerization (*tir-1*$^{\Delta SAM}$, *tir-1*$^{G747P}$ and *tir-*
1377 *1*$^{H833A}$) and NADase catalytic activity (*tir-1*$^{E788A}$) during *P. aeruginosa* infection **(B)**, following *nhr-*
1378 *8(RNAi)*, and during cholesterol deprivation **(D)**. Scale bars in all images equal 200 μm. **(E)**
1379 Immunoblot analysis of lysates from the indicated genotypes probed with antibodies targeting the
1380 doubly phosphorylated TGY epitope in phosphorylated PMK-1 (phos-PMK-1), total PMK-1 protein
1381 (total PMK-1), and tubulin (α-tubulin). *nsy-1(ag3)* and *pmk-1(km25)* loss-of-function mutants are
1382 the controls, which confirm the specificity of the phospho-PMK-1 probing. **(F)** The band intensities
1383 of three biological replicates of the Western blot shown in **(E)** were quantified. *equals $p<0.05$
1384 (one-way ANOVA with Dunnett multiple comparison testing). **(G)** qRT-PCR data of T24B8.5 in
1385 wild-type and mutant animals of the indicated genotypes grown on standard nematode growth
1386 media (+5 μg/mL cholesterol). Data are the average of three independent replicates, each
1387 normalized to a control gene with error bars representing SEM and are presented as the value
1388 relative to the average expression from all replicates in wild-type animals. *equals $p<0.05$ (two-
1389 way ANOVA with Tukey multiple comparison testing). **(H)** *C. elegans* pathogenesis assay with *P.*
1390 *aeruginosa* and *C. elegans* of indicated genotypes at the L4 larval stage are shown. Data are
1391 representative of three trials. The Kaplan-Meier method was used to estimate the survival curves
1392 for each group, and the log rank test was used for all statistical comparisons. Sample sizes, mean
1393 lifespan and p-values for all trials are shown in Table S2. See also Fig. S3.

1394 **Figure 4. The $NAD^+$ glycohydrolase activity of TIR-1/SARM1 is activated by a phase**
1395 **transition that requires TIR oligomerization. (A)** NADase activity of purified TIR at increasing
1396 TIR protein concentrations is shown. Activity was assessed by incubating TIR protein with 1 mM
1397 ε-NAD and monitoring the rate at which the fluorescent product ε-ADPR was produced. Curve
1398 represents a nonlinear regression fit of the NADase activity data points (n=2). **(B)** NADase activity
1399 of 2.5 μM TIR incubated in the presence of 25% (w/v) of macro- (PEG 8000, PEG 3350 and
1400 dextran) and micro- (sucrose and glycerol) viscogens was assessed as described in Fig. 4A (n=2).
1401 **(C)** Dose dependency of macroviscogens on the NADase activity of TIR is shown. 2.5 μM TIR
1402 protein was incubated with the indicated PEG compound at concentrations from 0-30% (w/v).
1403 NADase activity was assessed as described in Fig. 4A (n=2). **(D)** Steady-state kinetic analysis of
1404 2.5 μM TIR incubated in 0-30% (w/v) of PEG 3350 with the ε-NAD substrate provided at
1405 concentrations from 0-4000 μM was assessed as described in Fig. 4A. (n=2). From the steady-
1406 state kinetic analysis performed in Fig. 4D, $K_m$ **(E)**, $k_{cat}$ **(F)**, and $k_{cat}/K_m$ **(G)** were determined at
1407 each PEG 3350 concentration. **(H)** SDS-PAGE analysis of TIR protein fractions incubated with
1408 increasing concentrations of PEG 3350 before [precentrifugation (C)] and after centrifugation, the
1409 soluble (S) and pellet (P) protein fractions. NADase activity of TIR protein in each fraction and at
1410 each concentration of PEG 3350 was assessed, as described in Fig. 4A and is represented below
1411 the gel image (n=2, representative image shown). **(I)** Steady-state kinetic analysis of TIR wild-
1412 type, oligomerization mutant ($TIR^{G747P}$, $TIR^{H833A}$), and catalytic mutants ($TIR^{E788Q}$ and $TIR^{E788A}$) in
1413 25% PEG 3350 assessed with 0-2000 μM ε-NAD was assessed as described in Fig. 4D. Kinetic
1414 parameters ($K_m$, $k_{cat}$ and $k_{cat}/K_m$) are shown in the table below the graph (n=3). **(J, K)** SDS-PAGE
1415 analysis of TIR: wild-type, oligomerization mutant ($TIR^{G747P}$) and catalytic mutants ($TIR^{E788Q}$ and
1416 $TIR^{E788A}$), precipitation in the presence of 25% PEG 3350. Gel represents the soluble (S) and
1417 pellet (P) protein fractions of wild-type and mutant TIR following incubation with PEG 3350 and
1418 centrifugation. $TIR^{G747P}$ and $TIR^{E788Q}$ were assessed with 10 μM protein in Fig. 4J and $TIR^{E788A}$
1419 was assessed with 3 μM protein in Fig. 4K. Quantification of replicates represented below gel
1420 images (n=4, representative images shown). *equals $p<0.05$ by one-way ANOVA in Fig. 4J and
1421 unpaired t-test in Fig. 4K. See also Fig. S4.

1422 **Figure 5. A phase transition superactivates the intrinsic $NAD^+$ glycohydrolase of TIR. (A)**
1423 Effect of 1,6-hexanediol on TIR NADase activity is shown. TIR protein was incubated in the
1424 presence or absence of either 25% PEG 3350 or 500 mM citrate and treated with either 0 or 2%
1425 1,6-hexanediol. The NADase activity of TIR for each condition was assessed using the ε-NAD
1426 substrate assay (n=3). *equals $p<0.05$ (unpaired t-test). **(B)** The NADase activity of TIR protein
1427 incubated with either 25% PEG 3350 or 500 mM citrate before (precentrifugation, n=2) and after
1428 centrifugation, the supernatant (n=4) and precipitant (n=2) fractions. Precipitation fractions were
1429 resuspended in buffer alone or buffer containing 25% PEG 3350 or 500 mM citrate and NADase
1430 activity was assessed. **(C)** SDS-PAGE analysis of TIR protein in the soluble (S) and pellet (P)
1431 fractions following incubation with either PEG 3350 or citrate and centrifugation (1 spin). Pellet
1432 fractions were subsequently resuspended in only buffer or buffer containing 25% PEG 3350 or
1433 500 mM citrate and centrifuged a second time to isolate the soluble (S) and pellet (P) fractions
1434 (n=2, representative image shown). **(D)** SDS-PAGE analysis of TIR in the soluble (S) and pellet
1435 (P) fractions incubated with or without 25% PEG 3350 at the indicated pH (n=2, representative
1436 image shown). TIR steady state kinetic parameters [$K_m$ **(E)**, $k_{cat}$ **(F)**, $k_{cat}/K_m$ **(G)**] is shown at the
1437 indicated pH (n=2). **(H)** Negative stain electron microscopy in either the absence or presence of
1438 500 mM citrate (diameter of particles = 8.9 nm ± 1.2, n = 65). See also Fig. S5.

1439 **Figure 6. Physiologic stresses, both pathogen and non-pathogen, induce multimerization**
1440 **of TIR-1/SARM1 into visible puncta within intestinal epithelial cells. (A)** Images of animals
1441 expressing TIR-1::wrmScarlet in the indicated conditions. All *tir-1*::*wrmScarlet* animals were
1442 treated with *glo-3(RNAi)* to deplete autofluorescent gut granules. Representative images for each
1443 condition are displayed. Red fluorescent channel images display both TIR-1::wrmScarlet
1444 fluorescence and autofluorescent signal, while the green fluorescent channel only displays signals
1445 from autofluorescent gut granules. TIR-1::wrmScarlet puncta are indicated by arrowheads and
1446 autofluorescent gut granules by asterisks. **(B)** The number of puncta present in the last posterior
1447 pair of intestinal epithelial cells in both the red (*tir-1*::*wrmScarlet*) and green (autofluorescence)
1448 fluorescent channels were quantified using Fiji image analysis software. Each data point is the
1449 ratio of red/green puncta from one animal. The n is indicated for each condition. **(C)** Images of *tir-*
1450 *1*::*wrmScarlet* and *nhr-8(hd117)*;*tir-1::wrmScarlet* animals as described in (A) exposed to either
1451 0.1% Tergitol or *tir-1(RNAi)*. **(D)** Quantification of the ratio of red (TIR-1::wrmScarlet) to green
1452 (autofluorescence) puncta with indicated conditions as described in (B). Scale bar distance is
1453 indicated in all images. *equals $p<0.05$ by two-way ANOVA with Tukey multiple comparison
1454 testing.

1455 **Figure 7. Sterol scarcity primes p38 PMK-1 immune defenses. (A ,B, C, D, E)** Images of the
1456 indicated transcriptional immune reporters under the indicated conditions. Scale bars in all images
1457 equal 200 μm. **(F)** A heat map compares the expression levels of the 184 genes that were both
1458 induced in wild-type animals during *P. aeruginosa* infection and differentially expressed (either
1459 induced or repressed) in *nhr-8(hd117)* mutants at baseline (each greater than 2-fold, $q<0.05$). To
1460 compare expression of these genes in wild-type and *nhr-8(hd117)* mutants, we scaled the
1461 expression level in each condition by calculating a z-score for each row and performed
1462 hierarchical clustering, which identified two main clusters (Cluster I contains 139 genes and
1463 Cluster II contains 45 genes). See also Table S3. **(G)** Enrichment of p38 PMK-1-dependent genes
1464 in Cluster I and II genes is shown. **(H, I, J, K)** mRNA-seq data for the indicated genes from the
1465 experiment described in (F) showing scaled reads per base from three biological replicates.
1466 *equals $q<0.05$ from RNA-seq analysis. **(L)** Model of p38 PMK-1 pathway activation during sterol
1467 scarcity and pathogen infection.

1468 **Supplementary Figure 1. Cholesterol scarcity activates intestinal innate immune defenses.**
1469 **(A)** An mRNA-seq experiment as described in Fig. 1D, except using a different *nhr-8* mutant allele:
1470 *nhr-8(ok186)*. **(B)** Images of T24B8.5p::*gfp* animals as described in Fig. 1G. **(C)** Images of
1471 T24B8.5p::*gfp* on agarose media with 0.1% Tergitol in the presence of supplemented fatty acids,
1472 as indicated. See also Fig. 1.

1473 **Supplementary Figure 2. Cholesterol scarcity activates the p38 PMK-1 innate immune**
1474 **pathway. (A)** Gene set enrichment analysis (GSEA) of p38 PMK-1 targets in the mRNA-seq
1475 experiment as described in Fig 2D, except using a different *nhr-8* mutant allele: *nhr-8(ok186)*. **(B)**
1476 Images of T24B8.5p::*gfp* animals, as described in Fig. 2G. **(C)** Images of the transgenic *C.*
1477 *elegans*, in which *gfp* has been fused to the DAF-16 protein under the indicated conditions. Scale
1478 bars in all images equal 200 μm. See also Fig. 2.

1479 **Supplementary Figure 3. Activation of the p38 PMK-1 pathway by cholesterol deprivation**
1480 **requires TIR-1 oligomerization and NADase activity. (A)** qRT-PCR data of *irg-4* in wild-type
1481 and mutant animals as described in Fig. 3G. **(B)** Immunoblot analysis of lysates from the indicated
1482 genotypes probed with an antibody that recognizes the FLAG epitope. **(C)** Images of
1483 T24B8.5p::*gfp* immune reporter containing the indicated genotypes. Scale bars in all images
1484 equal 200 μm. See also Fig. 3.

1485 **Supplementary Figure 4. (A)** Enzyme concentration dependence in presence and absence of
1486 either 25% PEG 3350 or 500 mM sodium citrate (n=2). **(B)** Dose dependence of TIR NADase
1487 activity on citrate concentration as described in Fig. 4C, except using citrate (n=2). **(C)** Steady-
1488 state kinetic analysis of TIR as described in Fig. 4D, except in the presence of citrate (n=2). **(D-**
1489 **F)** From the steady-state kinetic analysis performed in Fig 4C, $K_m$ **(D)**, $k_{cat}$ **(E)**, and $k_{cat}/K_m$ **(F)** were
1490 determined at each citrate concentration. **(G)** Effect of citrate on TIR aggregation and associated
1491 activity as described in Fig. 4H (n=2, representative images shown). **(H)** Steady state kinetic
1492 analysis of TIR mutants as described in Fig. 4I, except in the presence of citrate (n=3). **(I, J)**
1493 Precipitation of TIR mutants as described in Fig. 4J and 4K, except in the presence of citrate (n=4,
1494 representative images shown). See also Fig. 4.

1495 **Supplementary Figure 5. (A)** SDS-PAGE analysis of TIR protein soluble (S) and pellet (P)
1496 fractions following TIR incubation first with 25% PEG 3350 or 500 mM citrate and subsequent
1497 addition of 2% 1,6-hexanediol (n=2, representative image shown). **(B)** SDS-PAGE analysis of TIR
1498 protein soluble (S) and pellet (P) fractions following TIR incubation first with 0 or 2% 1,6-
1499 hexanediol and subsequent addition of 25% PEG 3350 or 500 mM citrate (n=2, representative
1500 image shown). See also Fig. 5.

1501 **Supplementary Table S1. Genes significantly differentially expressed in *nhr-8(hd117)* and**
1502 ***nhr-8(ok186)* mutants compared to wild-type and in uninfected wild-type animals in the**
1503 **absence (0 µg/mL) versus presence (5 µg/mL) of cholesterol supplementation in the RNA-**
1504 **seq experiments presented in Figs. 1D, 1E and S1A.**
1505
1506 **Supplementary Table S2. Sample sizes, mean lifespan, and p values for the *C. elegans***
1507 **pathogenesis assays.**
1508
1509 **Supplementary Table S3. Genes in Cluster 1 and Cluster 2 of the heat map shown in Fig.**
1510 **6F.**
1511
1512 **Supplementary Table S4. Primer, crRNA guide and ssODN sequences designed for this**
1513 **study.**
1514

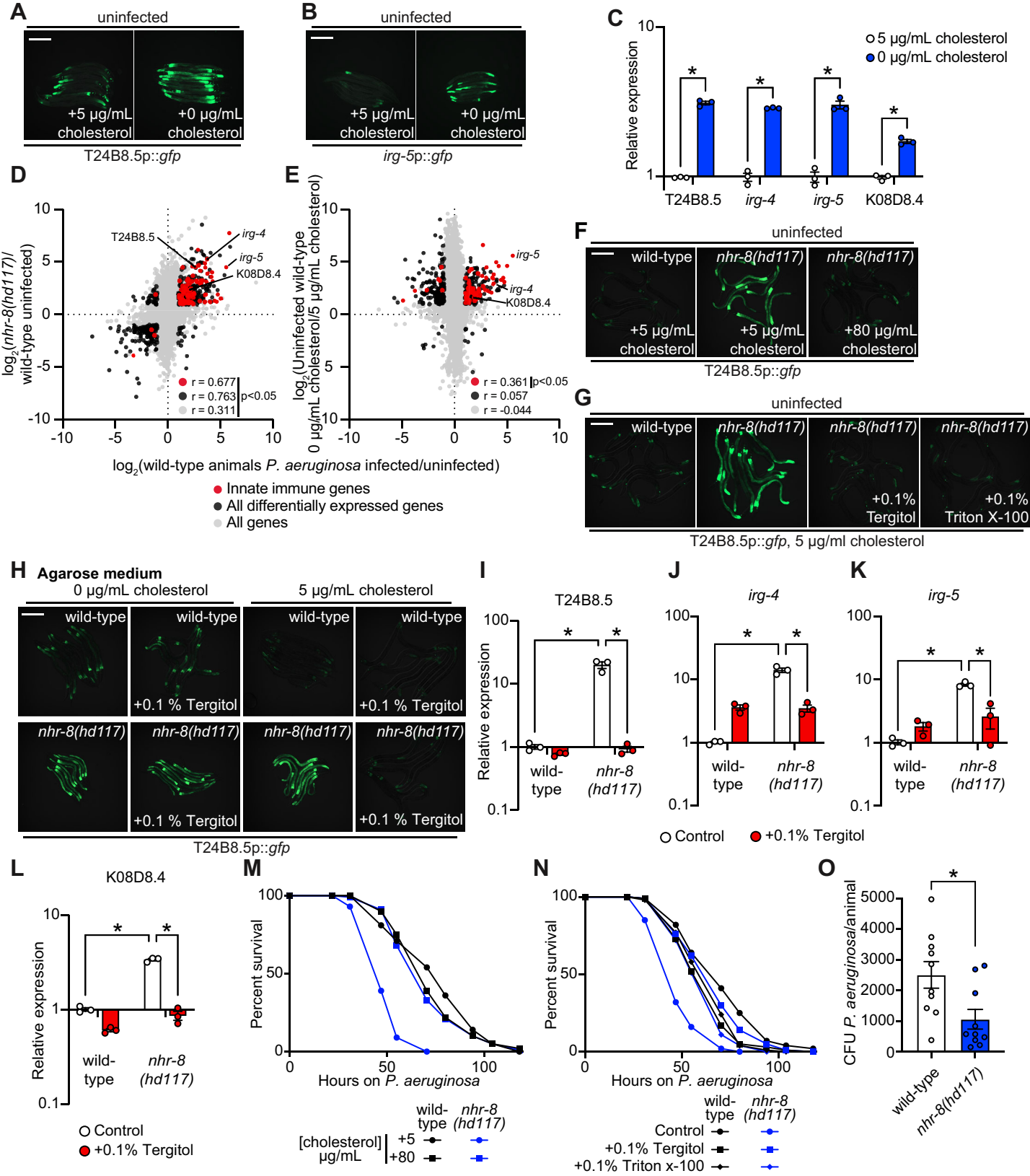
A
uninfected
+5 µg/mL cholesterol
+0 µg/mL cholesterol
T24B8.5p::gfp
B
uninfected
+5 µg/mL cholesterol
+0 µg/mL cholesterol
irg-5p::gfp
C
5 µg/mL cholesterol
0 µg/mL cholesterol
Relative expression
T24B8.5
irg-4
irg-5
K08D8.4
D
log2(nhr-8(hd117)/ wild-type uninfected)
T24B8.5
irg-4
irg-5
K08D8.4
r = 0.677
r = 0.763
r = 0.311
p<0.05
E
log2(Uninfected wild-type 0 µg/mL cholesterol/5 µg/mL cholesterol)
irg-5
irg-4
K08D8.4
r = 0.361
r = 0.057
r = -0.044
p<0.05
log2(wild-type animals P. aeruginosa infected/uninfected)
Innate immune genes
All differentially expressed genes
All genes
F
uninfected
wild-type
nhr-8(hd117)
nhr-8(hd117)
+5 µg/mL cholesterol
+5 µg/mL cholesterol
+80 µg/mL cholesterol
T24B8.5p::gfp
G
uninfected
wild-type
nhr-8(hd117)
nhr-8(hd117)
nhr-8(hd117)
+0.1% Tergitol
+0.1% Triton X-100
T24B8.5p::gfp, 5 µg/ml cholesterol
H
Agarose medium
0 µg/mL cholesterol
5 µg/mL cholesterol
wild-type
+0.1 % Tergitol
nhr-8(hd117)
T24B8.5p::gfp
I
T24B8.5
Relative expression
wild-type
nhr-8 (hd117)
J
irg-4
K
irg-5
Control
+0.1% Tergitol
L
K08D8.4
Relative expression
wild-type
nhr-8 (hd117)
Control
+0.1% Tergitol
M
Percent survival
Hours on P. aeruginosa
wild-type
nhr-8 (hd117)
[cholesterol] µg/mL
+5
+80
N
Percent survival
Hours on P. aeruginosa
wild-type
nhr-8 (hd117)
Control
+0.1% Tergitol
+0.1% Triton x-100
O
CFU P. aeruginosa/animal
wild-type
nhr-8(hd117)

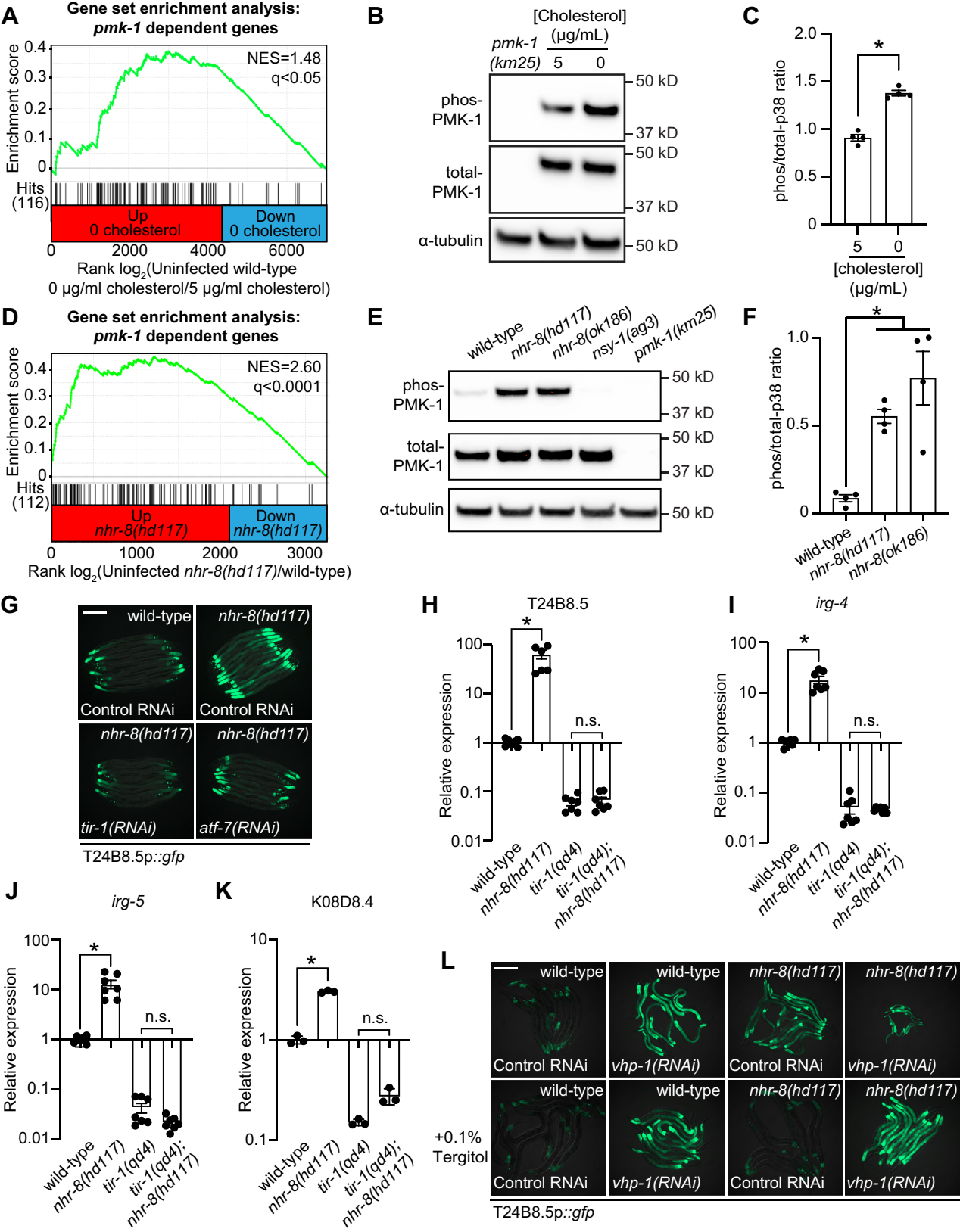
A
Gene set enrichment analysis:
pmk-1 dependent genes
NES=1.48
q<0.05
Enrichment score
Hits
(116)
Up
0 cholesterol
Down
0 cholesterol
Rank log2(Uninfected wild-type
0 µg/ml cholesterol/5 µg/ml cholesterol)
B
[Cholesterol]
(µg/mL)
pmk-1
(km25)
5
0
phos-
PMK-1
total-
PMK-1
α-tubulin
50 kD
37 kD
C
phos/total-p38 ratio
[cholesterol]
(µg/mL)
D
Gene set enrichment analysis:
pmk-1 dependent genes
NES=2.60
q<0.0001
Hits
(112)
Up
nhr-8(hd117)
Down
nhr-8(hd117)
Rank log2(Uninfected nhr-8(hd117)/wild-type)
E
wild-type
nhr-8(hd117)
nhr-8(ok186)
nsy-1(ag3)
pmk-1(km25)
F
G
wild-type
nhr-8(hd117)
Control RNAi
tir-1(RNAi)
atf-7(RNAi)
T24B8.5p::gfp
H
T24B8.5
Relative expression
n.s.
I
irg-4
J
irg-5
K
K08D8.4
L
+0.1%
Tergitol
vhp-1(RNAi)
T24B8.5p::gfp

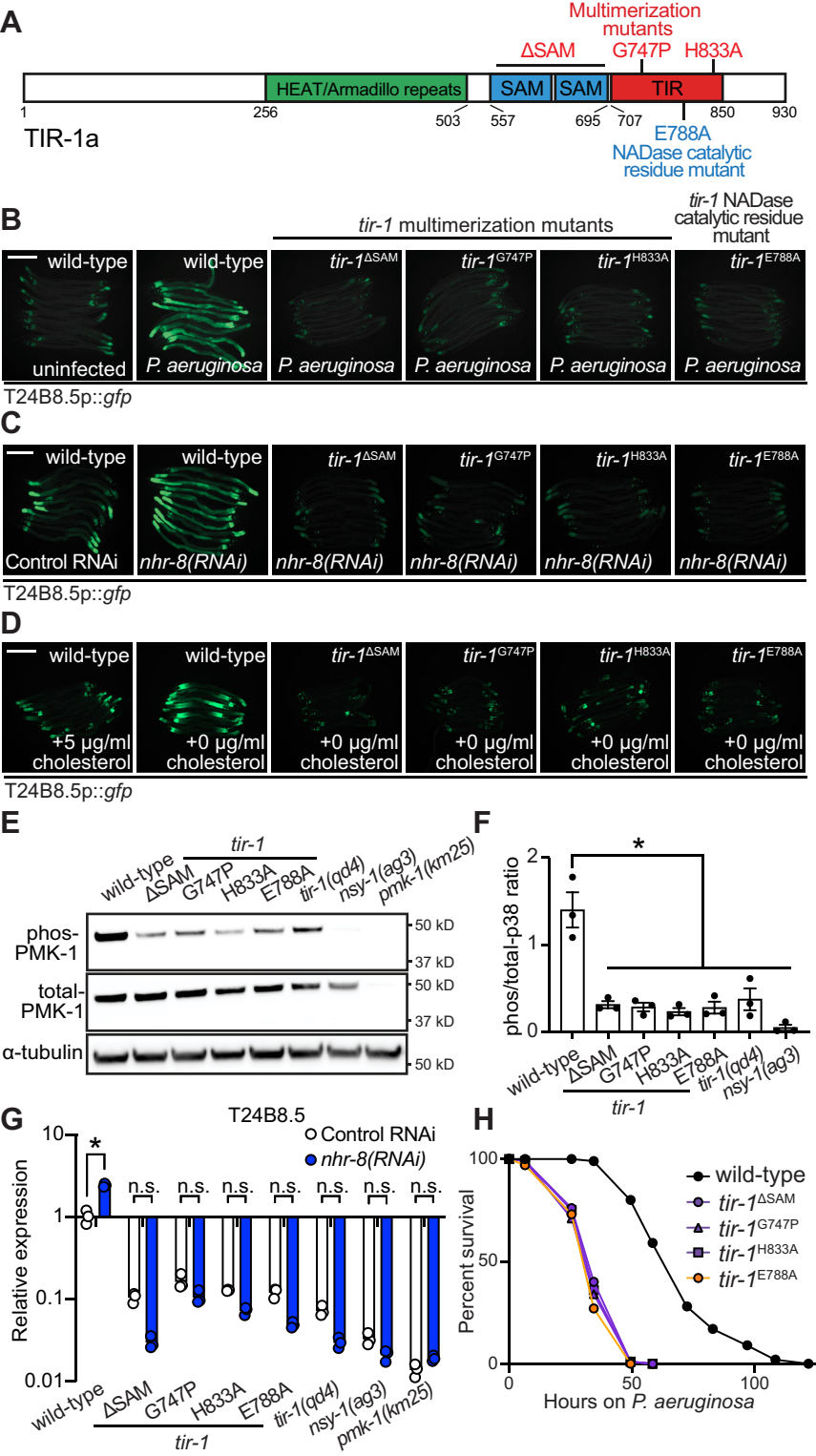
A
Multimerization mutants
ΔSAM
G747P
H833A
HEAT/Armadillo repeats
SAM
SAM
TIR
1
256
503
557
695
707
850
930
TIR-1a
E788A
NADase catalytic residue mutant
B
tir-1 multimerization mutants
tir-1 NADase catalytic residue mutant
wild-type
uninfected
wild-type
P. aeruginosa
tir-1ΔSAM
P. aeruginosa
tir-1G747P
P. aeruginosa
tir-1H833A
P. aeruginosa
tir-1E788A
P. aeruginosa
T24B8.5p::gfp
C
wild-type
Control RNAi
wild-type
nhr-8(RNAi)
tir-1ΔSAM
nhr-8(RNAi)
tir-1G747P
nhr-8(RNAi)
tir-1H833A
nhr-8(RNAi)
tir-1E788A
nhr-8(RNAi)
T24B8.5p::gfp
D
wild-type
+5 μg/ml cholesterol
wild-type
+0 μg/ml cholesterol
tir-1ΔSAM
+0 μg/ml cholesterol
tir-1G747P
+0 μg/ml cholesterol
tir-1H833A
+0 μg/ml cholesterol
tir-1E788A
+0 μg/ml cholesterol
T24B8.5p::gfp
E
tir-1
wild-type
ΔSAM
G747P
H833A
E788A
tir-1(qd4)
nsy-1(ag3)
pmk-1(km25)
phos-PMK-1
total-PMK-1
α-tubulin
50 kD
37 kD
50 kD
37 kD
50 kD
F
phos/total-p38 ratio
2
1
0
*
wild-type
ΔSAM
G747P
H833A
E788A
tir-1(qd4)
nsy-1(ag3)
tir-1
G
T24B8.5
Control RNAi
nhr-8(RNAi)
Relative expression
10
1
0.1
0.01
*
n.s.
wild-type
ΔSAM
G747P
H833A
E788A
tir-1(qd4)
nsy-1(ag3)
pmk-1(km25)
tir-1
H
Percent survival
100
50
0
wild-type
tir-1ΔSAM
tir-1G747P
tir-1H833A
tir-1E788A
0
50
100
Hours on P. aeruginosa

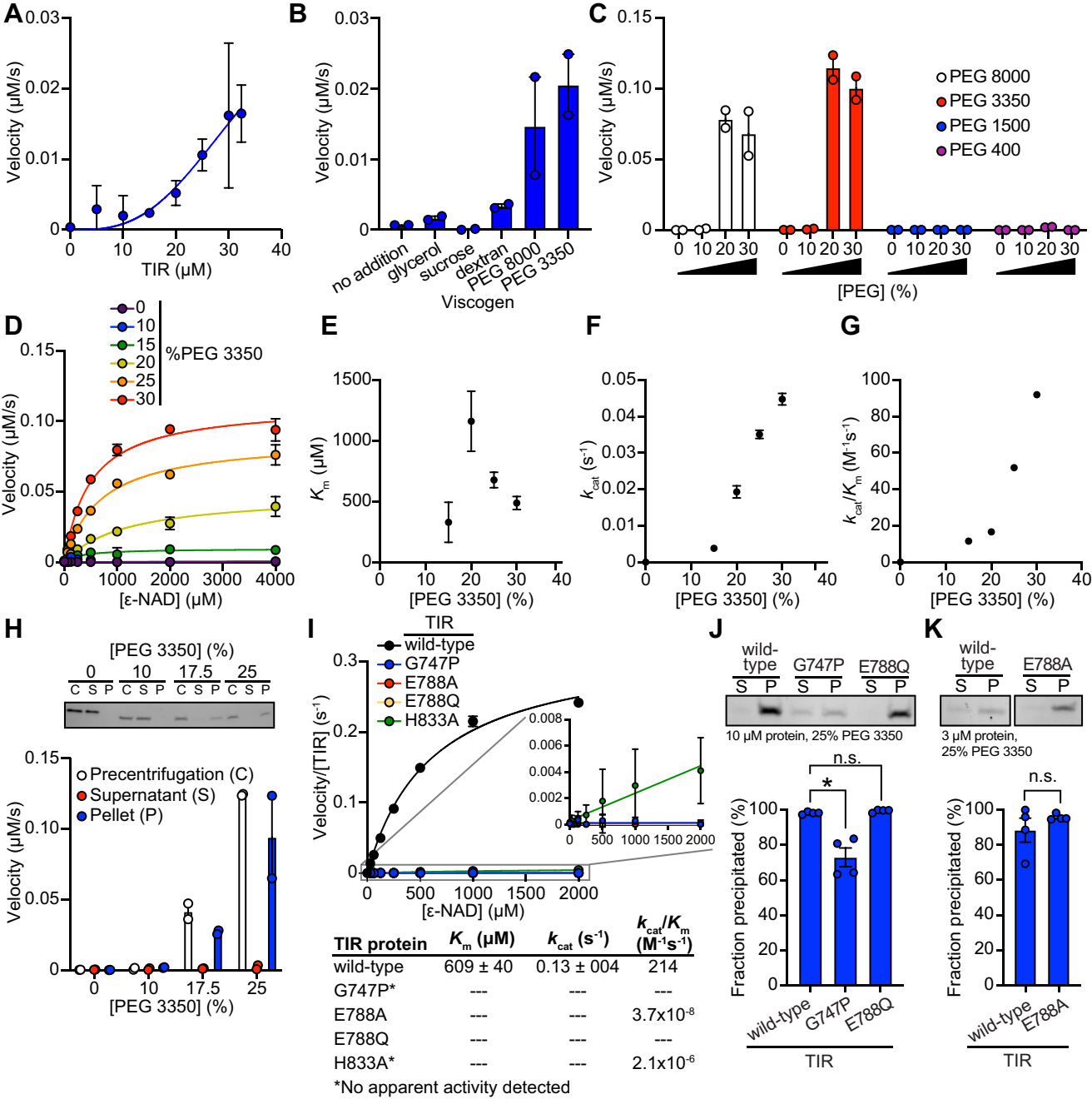


| TIR protein | $K_m$ (μM) | $k_{cat}$ (s$^{-1}$) | $k_{cat}/K_m$ (M$^{-1}$s$^{-1}$) |
|---|---|---|---|
| wild-type | 609 ± 40 | 0.13 ± 004 | 214 |
| G747P* | --- | --- | --- |
| E788A | --- | --- | 3.7x10$^{-8}$ |
| E788Q | --- | --- | --- |
| H833A* | --- | --- | 2.1x10$^{-6}$ |

*No apparent activity detected

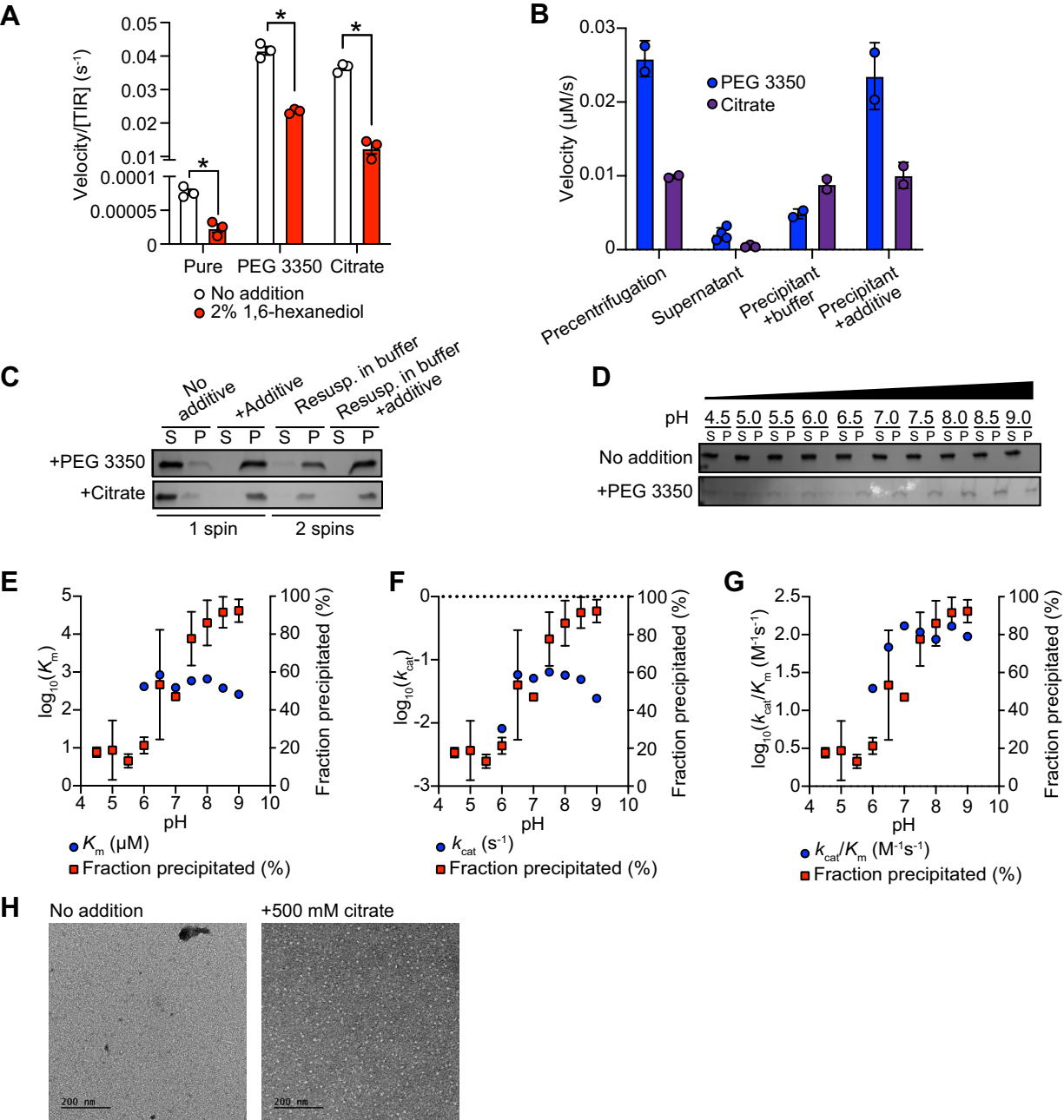
A
Velocity/[TIR] (s-1)
0.05
0.04
0.03
0.02
0.01
0.0001
0.00005
0
*
*
*
Pure
PEG 3350
Citrate
No addition
2% 1,6-hexanediol
B
Velocity (μM/s)
0.03
0.02
0.01
0
PEG 3350
Citrate
Precentrifugation
Supernatant
Precipitant +buffer
Precipitant +additive
C
No additive
+Additive
Resusp. in buffer
Resusp. in buffer +additive
S P S P S P S P
+PEG 3350
+Citrate
1 spin
2 spins
D
pH 4.5 5.0 5.5 6.0 6.5 7.0 7.5 8.0 8.5 9.0
S P S P S P S P S P S P S P S P S P S P
No addition
+PEG 3350
E
log10(Km)
Fraction precipitated (%)
pH
Km (μM)
Fraction precipitated (%)
F
log10(kcat)
Fraction precipitated (%)
pH
kcat (s-1)
Fraction precipitated (%)
G
log10(kcat/Km (M-1s-1)
Fraction precipitated (%)
pH
kcat/Km (M-1s-1)
Fraction precipitated (%)
H
No addition
+500 mM citrate
200 nm
200 nm

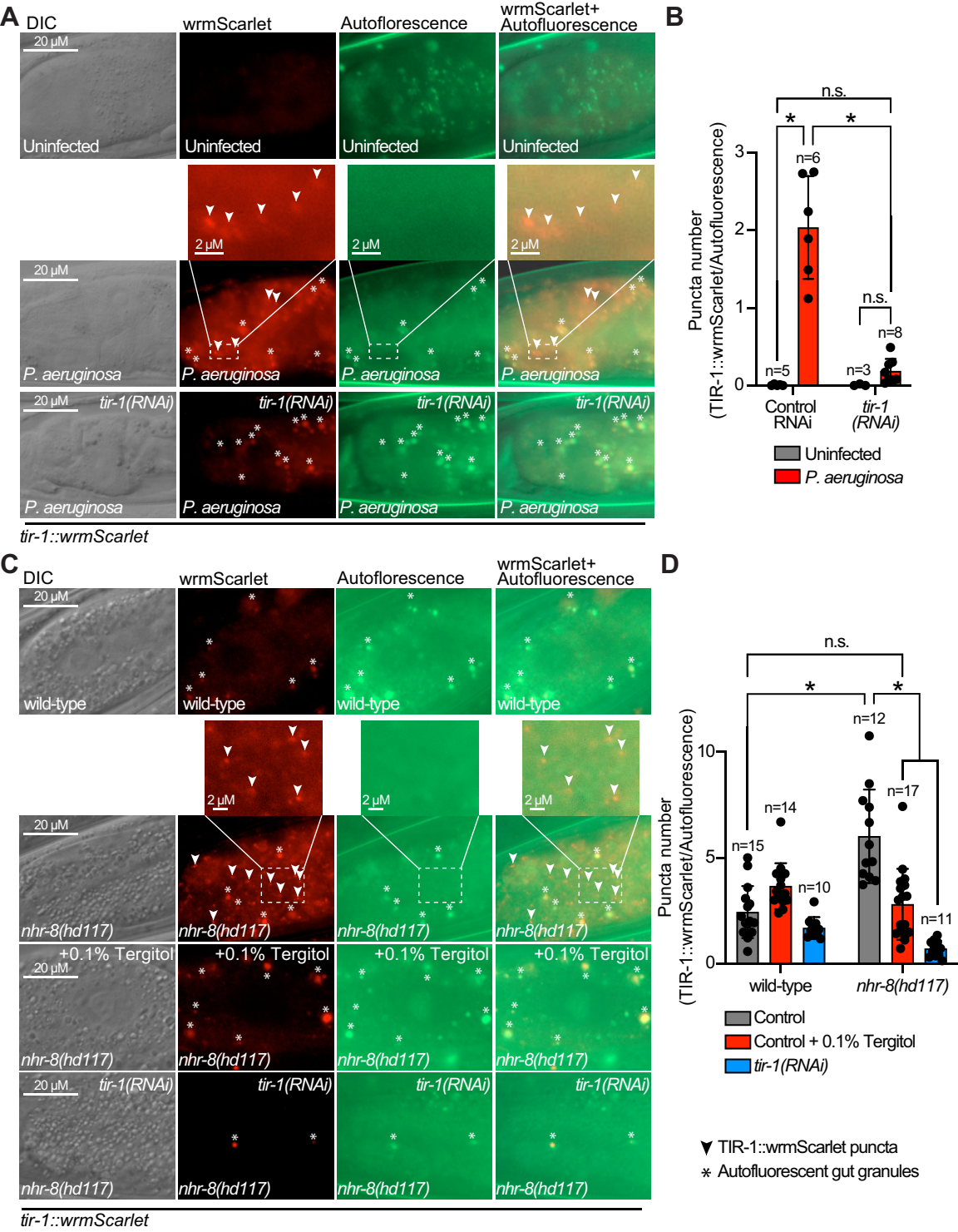
A
DIC
wrmScarlet
Autoflorescence
wrmScarlet+ Autofluorescence
20 µM
Uninfected
2 µM
P. aeruginosa
tir-1(RNAi)
tir-1::wrmScarlet
B
n.s.
*
*
n=6
n=5
n=3
n=8
Puncta number (TIR-1::wrmScarlet/Autofluorescence)
Control RNAi
tir-1 (RNAi)
Uninfected
P. aeruginosa
C
wild-type
nhr-8(hd117)
+0.1% Tergitol
D
n=15
n=14
n=10
n=12
n=17
n=11
Control
Control + 0.1% Tergitol
TIR-1::wrmScarlet puncta
Autofluorescent gut granules

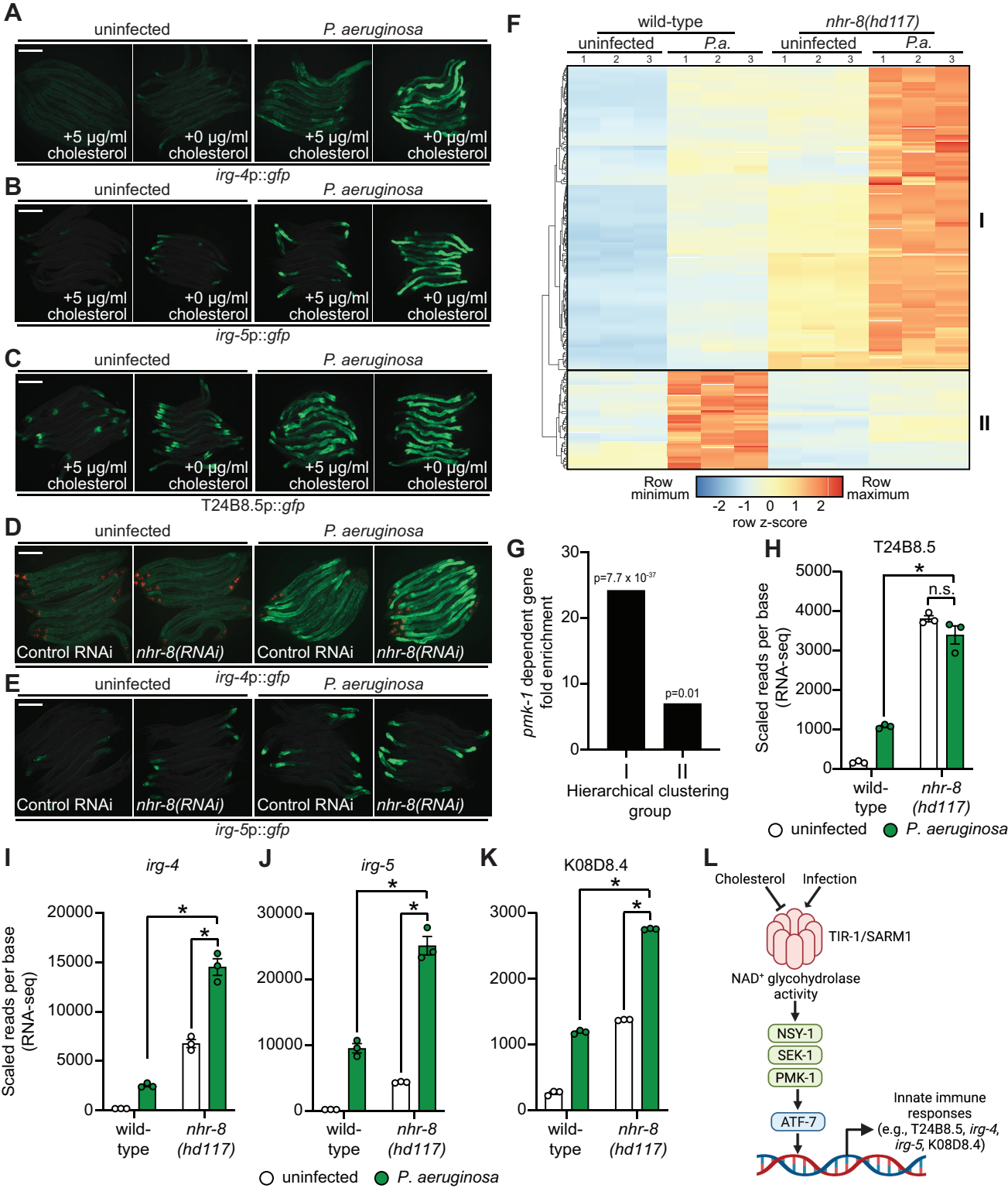
A
uninfected
P. aeruginosa
+5 µg/ml cholesterol
+0 µg/ml cholesterol
irg-4p::gfp
B
irg-5p::gfp
C
T24B8.5p::gfp
D
Control RNAi
nhr-8(RNAi)
E
F
wild-type
nhr-8(hd117)
P.a.
I
II
Row minimum
Row maximum
row z-score
G
pmk-1 dependent gene fold enrichment
p=7.7 x 10-37
p=0.01
Hierarchical clustering group
H
T24B8.5
Scaled reads per base (RNA-seq)
n.s.
wild-type
nhr-8 (hd117)
uninfected
P. aeruginosa
I
irg-4
J
irg-5
K
K08D8.4
L
Cholesterol
Infection
TIR-1/SARM1
NAD+ glycohydrolase activity
NSY-1
SEK-1
PMK-1
ATF-7
Innate immune responses (e.g., T24B8.5, irg-4, irg-5, K08D8.4)